J. Fluid Mech. (2021), *vol*. 929, A33, doi:10.1017/jfm.2021.875

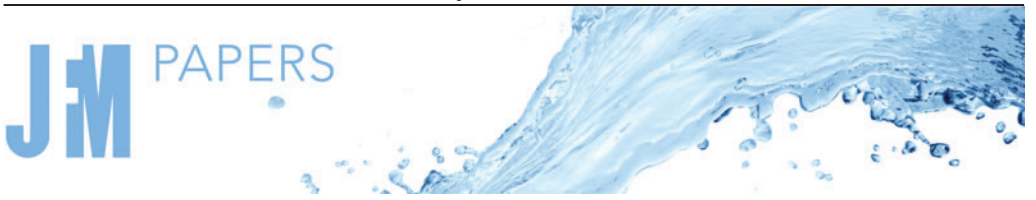

Effect of wall temperature on the kinetic energy transfer in a hypersonic turbulent boundary layer

Dehao Xu[1], Jianchun Wang[2,†], Minping Wan[2], Changping Yu[3], Xinliang Li[3] and Shiyi Chen[1,2,†]

[1]State Key Laboratory of Turbulence and Complex Systems, College of Engineering, Peking University, Beijing 100871, PR China

[2]Guangdong Provincial Key Laboratory of Fundamental Turbulence Research and Applications, Center for Complex Flows and Soft Matter Research, Department of Mechanics and Aerospace Engineering, Southern University of Science and Technology, Shenzhen 518055, PR China

[3]Laboratory of High Temperature Gas Dynamics, Institute of Mechanics, Chinese Academy of Sciences, Beijing 100190, PR China

(Received 10 March 2021; revised 26 July 2021; accepted 4 October 2021)

The effect of wall temperature on the transfer of kinetic energy in a hypersonic turbulent boundary layer for different Mach numbers and wall temperature ratios is studied by direct numerical simulation. A cold wall temperature can enhance the compressibility effect in the near-wall region through increasing the temperature gradient and wall heat flux. It is shown that the cold wall temperature enhances the local reverse transfer of kinetic energy from small scales to large scales, and suppresses the local direct transfer of kinetic energy from large scales to small scales. The average filtered spatial convection and average filtered viscous dissipation are dominant in the near-wall region, while the average subgrid-scale flux of kinetic energy achieves its peak value in the buffer layer. It is found that the wall can suppress the inter-scale transfer of kinetic energy, especially for the situation of a cold wall. A strong local reverse transfer of fluctuating kinetic energy is identified in the buffer layer in the inertial range. Helmholtz decomposition is applied to analyse the compressibility effect on the subgrid-scale flux of kinetic energy. A strong transfer of the solenoidal component of fluctuating kinetic energy is identified in the buffer layer, while a significant transfer of the dilatational component of fluctuating kinetic energy is observed in the near-wall region. It is also shown that compression motions have a major contribution to the direct transfer of fluctuating kinetic energy, while expansion motions play a marked role in the reverse transfer of fluctuating kinetic energy.

Key words: compressible boundary layers, hypersonic flow

† Email addresses for correspondence: wangjc@sustech.edu.cn, chensy@sustech.edu.cn

1. Introduction

Study of supersonic and hypersonic turbulent boundary layers is of extraordinary importance in the aerospace industry (Cebeci & Smith 1974; Smits & Dussauge 2006; Gatski & Bonnet 2009). Much work has been devoted to understanding the mechanism of the compressible turbulent boundary layer. A boundary layer is essentially a spatially developing flow, and is sensitive to the set-up of inflow boundary conditions. As shown by Erm & Joubert (1991) and Simens *et al.* (2009), extremely long computational domains are required to achieve the fully developed state of the turbulent boundary layer and avoid the artificial effect of inflow boundary conditions. Furthermore, due to the remarkable influence of compressibility, supersonic and hypersonic turbulent boundary layers are more complex than an incompressible turbulent boundary layer (Bradshaw 1977; Guarini *et al.* 2000; Maeder, Adams & Kleiser 2001; Pirozzoli, Grasso & Gatski 2004; Martin 2007; Pirozzoli, Bernardini & Grasso 2008; Ringuette, Wu & Martin 2008; Duan, Beekman & Martin 2010; Pirozzoli, Bernardini & Grasso 2010; Duan, Beekman & Martin 2011; Lagha *et al.* 2011; Pirozzoli & Bernardini 2011; Li & Coleman 2012; Pirozzoli 2012; Wang & Lu 2012; Zhang *et al.* 2012; Chu & Lu 2013; Chu, Zhuang & Lu 2013; Liang & Li 2013; Marco *et al.* 2013; Zhang *et al.* 2014; Alizard *et al.* 2015; Liang & Li 2015; She *et al.* 2018; Li *et al.* 2019). The eddy shocklets in turbulence and large temperature gradients across the boundary layer bring great challenges for numerical simulations. Moreover, it is worth noting that several inflow boundary conditions were applied in previous direct numerical simulation (DNS) studies, including an extended temporal method with the streamwise periodic boundary condition (Guarini *et al.* 2000; Maeder *et al.* 2001), a method that simulates the entire boundary layer transition process from laminar inflow condition into the fully developed turbulent state (Pirozzoli *et al.* 2004), a recycling–rescaling method (Duan *et al.* 2010; Lagha *et al.* 2011) and a synthetic eddy method (Li & Coleman 2012).

One of the most important differences between supersonic and hypersonic turbulent boundary layers is the wall temperature condition (Duan *et al.* 2010; Chu *et al.* 2013). If an aircraft flies at a supersonic speed, the wall temperature is essentially considered as adiabatic, while for an aircraft at a hypersonic speed, the wall temperature is markedly lower than the adiabatic wall temperature (Duan *et al.* 2010; Chu *et al.* 2013). Duan *et al.* (2010) performed DNS of a turbulent boundary layer at Mach number 5 with isothermal boundary condition. The ratio of the wall to the edge temperature T_w/T_δ ranges from 1.0 to 5.4. They investigated the influence of cold wall temperature on Morkovin's scaling and the strong Reynolds analogy. They showed that many scaling relations for isothermal compressible turbulent boundary layer are nearly the same as those found in adiabatic cases, and the compressibility effect is insignificantly enhanced by cold wall temperature. Liang & Li (2013) performed DNS of a spatially evolving hypersonic turbulent boundary layer at Mach number 8 with isothermal cold wall condition. They found that high Mach number and cold wall temperature can induce a strong compressibility effect.

According to the energy cascade hypothesis of three-dimensional fully developed turbulence, in the statistical sense, kinetic energy is injected to turbulence at large scales, and then transferred to smaller scales until dissipated by viscous action at small scales close to the Kolmogorov length scale (Meneveau & Katz 2000; Pope 2000). However, a backscatter of energy also occurs locally, and can be identified as negative values of the subgrid-scale (SGS) flux in the filtered kinetic energy equation. The existence of local reverse transfer of kinetic energy from small scales to large scales represents a great challenge to large-eddy simulation (LES) of turbulence. An overestimation of the backscatter of kinetic energy can result in numerical instability, while an underestimation

of energy backscatter can give rise to excessive SGS dissipation. The investigation of the mechanism of the energy transfer across different scales is very important for improving the SGS models in LES (Wang *et al.* 2018).

Inter-scale kinetic energy transfer has been extensively investigated in incompressible turbulence (Piomelii *et al.* 1991; Domaradzki, Liu & Brachet 1993; Kerr, Domaradzki & Barbier 1996; Cerutti & Meneveau 1998; Eyink 2005; Aluie & Eyink 2009; Eyink & Aluie 2009). Piomelii *et al.* (1991) performed DNS of transitional and turbulent channel flow as well as compressible isotropic turbulence. They pointed out that accurate modelling of the backscatter phenomenon is crucial for LES of turbulence. Domaradzki *et al.* (1993) and Kerr *et al.* (1996) analysed the SGS energy transfer in both spectral and physical space for incompressible isotropic turbulence. The forward and inverse energy transfers are both significant in the dynamics of resolved scales. Localness of energy cascade in incompressible turbulence has been systematically investigated by Eyink (2005), Eyink & Aluie (2009) and Aluie & Eyink (2009). However, for compressible turbulence, the mechanism of inter-scale kinetic energy transfer is relatively less investigated (Aluie 2011; Aluie, Li & Li 2012; Aluie 2013; Wang *et al.* 2013, 2018; Teng *et al.* 2021; Zheng *et al.* 2021). Aluie (2011, 2013) pointed out that inter-scale transfer of kinetic energy in compressible turbulence is dominated by local interactions, provided that the pressure-dilatation co-spectrum decays at a sufficiently rapid rate. The conclusion was further verified by numerical simulations of both forced and decaying compressible isotropic turbulence (Aluie *et al.* 2012). Wang *et al.* (2013) performed numerical simulation of compressible isotropic turbulence by applying large-scale forces to both solenoidal and dilatational components of the velocity field. They found that the SGS kinetic energy flux of the dilatational mode is significantly larger than that of the solenoidal mode in the inertial range, due to the effect of sheet-like shock waves of large scale generated in the simulated flow. Furthermore, Wang *et al.* (2018) performed numerical simulation of compressible isotropic turbulence with solenoidal forcing at turbulent Mach numbers ranging from 0.4 to 1.0. They reported that compression motions enhance the positive SGS flux of kinetic energy, and expansion motions enhance the negative SGS flux of kinetic energy. They also applied Helmholtz decomposition to investigate the inter-scale transfer of solenoidal and dilatational components of kinetic energy. They found that the SGS flux of solenoidal kinetic energy is insensitive to the change of turbulent Mach number, while the SGS flux of dilatational kinetic energy increases drastically as the turbulent Mach number becomes larger.

The mechanism of a supersonic turbulent boundary layer with adiabatic boundary condition has been widely investigated. However, due to a larger computational cost and occurrence of strong shock waves, the structures and statistics of hypersonic turbulent boundary layers with isothermal wall condition are scarcely investigated. Previous works (Duan *et al.* 2010; Chu *et al.* 2013; Liang & Li 2013) were concentrated on some statistical relations of flow fields, including the Van Driest transformation of mean velocity profiles, Walz's relation, Morkovin's scaling and the strong Reynolds analogy, which are valid when the free-stream Mach number $M \approx 5$ and partly valid for $M = 8$. However, the effect of wall temperature on kinetic energy transfer in hypersonic turbulent boundary layers has never been studied.

Helmholtz decomposition has been used in the analysis of compressible isotropic turbulence (Wang *et al.* 2018, 2020; Teng *et al.* 2020; Zheng *et al.* 2020), homogeneous shear turbulent flows (Chen *et al.* 2018, 2019*a*,*b*; Wang *et al.* 2020) and turbulent channel flows (Yu, Xu & Pirozzoli 2019; Yu & Xu 2021). Furthermore, Helmholtz decomposition has also been applied in supersonic turbulent boundary layers by Pirozzoli *et al.* (2010),

where the dilatational component has been ignored. Recently, Xu *et al.* (2021) employed Helmholtz decomposition in the numerical study of hypersonic turbulent boundary layers. The statistical properties of dilatational components of flow fields were investigated to demonstrate the compressibility effect in a hypersonic turbulent boundary layer with isothermal wall condition.

In this study, we investigate the inter-scale transfer of kinetic energy in a hypersonic turbulent boundary layer. The effects of compressibility and wall temperature on the SGS flux of kinetic energy are discussed aiming to give guidance on the LES modelling of hypersonic turbulent boundary layers. The rest of the paper is organized as follows. The governing equations and numerical methodology are described in § 2. The dynamic equations of the filtered kinetic energy are derived in § 3. Numerical results for the inter-scale transfer of kinetic energy are presented in § 4. The mean-fluctuating decomposition and Helmholtz decomposition of the inter-scale transfer of kinetic energy are presented in § 5. Finally, a summary is given and conclusions are drawn in § 6.

2. Governing equations and numerical methodology

A set of reference scales are introduced to normalize the variables in compressible turbulence (Wang *et al.* 2012*a*,*b*; Liang & Li 2013, 2015). The reference length L_∞, free-stream velocity U_∞, density ρ_∞, pressure $p_\infty = \rho_\infty U_\infty^2$, free-stream temperature T_∞, energy per unit volume $\rho_\infty U_\infty^2$, viscosity μ_∞ and thermal conductivity κ_∞ are utilized. Thus, three non-dimensional governing parameters appear: the Reynolds number $Re = \rho_\infty U_\infty L_\infty/\mu_\infty$, the Mach number $M = U_\infty/c_\infty$ and the Prandtl number $Pr = \mu_\infty C_p/\kappa_\infty$. Ratio $\gamma = C_p/C_v$ is the ratio of specific heat at constant pressure C_p to that at constant volume C_v, which is assumed to be equal to 1.4. The parameter α is defined as $\alpha = PrRe(\gamma - 1)M^2$, where Pr is assumed to be equal to 0.7.

The following dimensionless Navier–Stokes equations in conservation form are solved numerically (Wang *et al.* 2018, 2020):

$$\frac{\partial \rho}{\partial t} + \frac{\partial(\rho u_j)}{\partial x_j} = 0, \tag{2.1}$$

$$\frac{\partial(\rho u_i)}{\partial t} + \frac{\partial[\rho u_i u_j + p\delta_{ij}]}{\partial x_j} = \frac{1}{Re}\frac{\partial \sigma_{ij}}{\partial x_j}, \tag{2.2}$$

$$\frac{\partial E}{\partial t} + \frac{\partial[(E+p)u_j]}{\partial x_j} = \frac{1}{\alpha}\frac{\partial}{\partial x_j}\left(\kappa\frac{\partial T}{\partial x_j}\right) + \frac{1}{Re}\frac{\partial(\sigma_{ij}u_i)}{\partial x_j}, \tag{2.3}$$

$$p = \rho T/(\gamma M^2), \tag{2.4}$$

where u_i is the velocity component, ρ is the density, p is the pressure and T is the temperature. Parameter σ_{ij} is the viscous stress and is defined as

$$\sigma_{ij} = \mu\left(\frac{\partial u_i}{\partial x_j} + \frac{\partial u_j}{\partial x_i}\right) - \tfrac{2}{3}\mu\theta\delta_{ij}, \tag{2.5}$$

where $\theta = \partial u_k/\partial x_k$ is the velocity divergence. The total energy per unit volume E is

$$E = \frac{p}{\gamma - 1} + \tfrac{1}{2}\rho(u_j u_j). \tag{2.6}$$

The convection terms in the above governing equations are approximated by a seventh-order weighted essentially non-oscillatory scheme (Balsara & Shu 2000), while

Case	M_∞	Re_∞	T_w/T_∞	T_w/T_r	$L_x \times L_y \times L_z$	$N_x \times N_y \times N_z$
M6T04	6	2×10^6	3.0	0.4	$16 \times 0.7 \times 0.2$	$7000 \times 200 \times 640$
M6T08	6	2×10^6	6.0	0.8	$16 \times 0.7 \times 0.2$	$6000 \times 200 \times 320$
M8T015	8	2×10^6	1.9	0.15	$19 \times 0.7 \times 0.35$	$9000 \times 200 \times 1280$
M8T04	8	2×10^6	5.0	0.4	$17 \times 0.7 \times 0.2$	$7000 \times 200 \times 320$
M8T08	8	5×10^6	10.03	0.8	$41 \times 0.7 \times 0.6$	$12\,500 \times 200 \times 640$

Case	Δx^+	Δy_w^+	Δz^+	x_a	δ	N	T_f	T_{all}
M6T04	9.3	0.5	3.6	12	0.15	200	$140\delta/U_\infty$	7.0×10^5
M6T08	4.9	0.5	3.1	12	0.14	200	$140\delta/U_\infty$	3.0×10^5
M8T015	11.2	0.5	4.5	14	0.13	200	$150\delta/U_\infty$	1.8×10^6
M8T04	5.6	0.5	3.5	13	0.14	200	$140\delta/U_\infty$	3.5×10^5
M8T08	12.2	0.5	4.6	30	0.28	200	$140\delta/U_\infty$	1.3×10^6

Table 1. Summary of computational parameters for the DNS study. The computational domains L_x, L_y and L_z are non-dimensionalized by 1 inch (Pirozzoli *et al.* 2004).

the viscous terms are discretized by an eighth-order central difference scheme. A third- order total variation diminishing type of Runge–Kutta method is applied for time advancing (Liang & Li 2013).

According to Helmholtz decomposition, the velocity field ($\boldsymbol{u}$) can be decomposed into a solenoidal ($\boldsymbol{u}_s$) and a dilatational ($\boldsymbol{u}_d$) component ($\boldsymbol{u} = \boldsymbol{u}_s + \boldsymbol{u}_d$), which respectively satisfy $\boldsymbol{\nabla} \cdot \boldsymbol{u}_s = 0$ and $\boldsymbol{\nabla} \times \boldsymbol{u}_d = 0$. The two components can be obtained from the velocity field $\boldsymbol{u}$ by solving Possion equations of the vector potential $\boldsymbol{A}$ and scalar potential φ:

$$\nabla^2 \boldsymbol{A} = -\boldsymbol{\nabla} \times \boldsymbol{u}, \quad \nabla^2 \varphi = \boldsymbol{\nabla} \cdot \boldsymbol{u}. \tag{2.7a,b}$$

Then, the solenoidal and dilatational components can be obtained by

$$\boldsymbol{u}_s = \boldsymbol{\nabla} \times \boldsymbol{A}, \quad \boldsymbol{u}_d = \boldsymbol{\nabla} \varphi. \tag{2.8a,b}$$

According to Hirasaki & Hellums (1970), with the wall boundary conditions

$$\frac{\partial \varphi}{\partial y} = 0, \quad \frac{\partial A_y}{\partial y} = 0, \quad A_x = A_z = 0, \tag{2.9a–c}$$

the vector potential $\boldsymbol{A}$ is unique (Hirasaki & Hellums 1970; Pirozzoli *et al.* 2010; Yu *et al.* 2019). A mirror symmetry is applied to the data in a large streamwise window of $[x_a - 4\delta, x_a + 4\delta]$ to generate an artificial periodic condition in the streamwise direction. Then, the Poisson equations (2.7*a*,*b*) are discretized spectrally in the streamwise (x) and spanwise (z) directions, and by a sixth-order central difference in the wall-normal (y) direction. It is worth noting that the artificial periodic condition has no effect on the flow statistics of the data in a small streamwise window of $[x_a - 0.5\delta, x_a + 0.5\delta]$. If the streamwise window is further increased to $[x_a - 8\delta, x_a + 8\delta]$, the flow statistics of the data in $[x_a - 0.5\delta, x_a + 0.5\delta]$ are unchanged. Here x_a is the streamwise location in the hypersonic turbulent boundary layer and δ is the boundary layer thickness. The values of x_a and δ are listed in table 1. It should be noted that the Helmholtz decomposition has been validated in Xu *et al.* (2021).

In this study, f_{ra} represents the Reynolds average (spanwise and time average) of f, and the fluctuating counterpart of the Reynolds average is defined as $f' = f - f_{ra}$.

Moreover, $f_{fa} = (\rho f)_{ra}/\rho_{ra}$ denotes the Favre average (spanwise and time average) of f. The fluctuating counterpart is $f'' = f - f_{fa}$.

The governing equation of kinetic energy is given by (Wang *et al.* 2018, 2020)

$$\frac{\partial}{\partial t}\left(\tfrac{1}{2}\rho u_i^2\right) = -J - \Phi - D, \tag{2.10}$$

where J is the spatial convection term, Φ is the pressure dilatation term and D is the viscous dissipation term. These terms can be written as

$$J = \frac{\partial}{\partial x_j}\left(\tfrac{1}{2}\rho u_i^2 u_j + p u_j - \frac{u_i \sigma_{ij}}{Re}\right), \tag{2.11}$$

$$\Phi = -p\frac{\partial u_i}{\partial x_i} = -p\theta, \tag{2.12}$$

$$D = \frac{\sigma_{ij}}{Re}\frac{\partial u_i}{\partial x_j} = \frac{\sigma_{ij} S_{ij}}{Re}, \tag{2.13}$$

where θ is the velocity divergence and $S_{ij} = (1/2)(\partial u_i/\partial x_j + \partial u_j/\partial x_i)$ is the strain-rate tensor.

The average of kinetic energy can be derived as

$$\frac{\partial}{\partial t}\left\langle \tfrac{1}{2}\rho u_i^2 \right\rangle = -\langle J\rangle - \langle \Phi\rangle - \langle D\rangle. \tag{2.14}$$

Here $\langle f\rangle$ represents the average of variable f in streamwise, wall-normal and spanwise directions and time. Also, $\varepsilon \equiv \langle D\rangle$ is the average of viscous dissipation.

3. Dynamic equations of the filtered kinetic energy

In the following sections, the filtered method is used to investigate the effects of compressibility and wall temperature on the inter-scale transfer of kinetic energy.

The filtered field for a variable f can be defined as

$$\bar{f}(\boldsymbol{x}) = \int d^3\boldsymbol{r} G_l(\boldsymbol{r}) f(\boldsymbol{x}+\boldsymbol{r}), \tag{3.1}$$

where $G_l(\boldsymbol{r}) \equiv l^{-3}G(\boldsymbol{r}/l)$ is the filter function, and $G(\boldsymbol{r})$ is a normalized window function. Here, l is the filter width associated with the wavelength of the smallest scale retained by the filtering operation. The symbol $\tilde{f} = \overline{\rho f}/\bar{\rho}$ represents the Favre filtered field. In the present study, the top-hat filter is used, which can be calculated in one dimension by (Martin *et al.* 2000; Wang *et al.* 2018)

$$\bar{f} = \frac{1}{4n}\left(f_{i-n} + 2\sum_{j=i-n+1}^{i+n-1} f_j + f_{i+n}\right), \tag{3.2}$$

where the filter width is $l = 2n\Delta x$. It should be noted that in order to precisely investigate the properties of the inter-scale transfer of kinetic energy along the wall-normal direction, the filtering technique is only applied on the streamwise and spanwise directions, that is, no filter is employed for the wall-normal direction.

The filtered equations for the density and momentum are (Wang *et al.* 2018, 2020)

$$\frac{\partial \bar{\rho}}{\partial t} + \frac{\partial (\bar{\rho}\tilde{u}_j)}{\partial x_j} = 0, \tag{3.3}$$

$$\frac{\partial (\bar{\rho}\tilde{u}_i)}{\partial t} + \frac{\partial [\bar{\rho}\tilde{u}_i\tilde{u}_j + \bar{p}\delta_{ij}]}{\partial x_j} = -\frac{\partial (\bar{\rho}\tilde{\tau}_{ij})}{\partial x_j} + \frac{1}{Re}\frac{\partial \bar{\sigma}_{ij}}{\partial x_j}, \tag{3.4}$$

where the SGS stress is $\bar{\rho}\tilde{\tau}_{ij} = \bar{\rho}(\widetilde{u_i u_j} - \tilde{u}_i\tilde{u}_j)$. Thus, it is straightforward to derive the filtered equation for the filtered kinetic energy $(1/2)\bar{\rho}\tilde{u}_i^2$ (Aluie 2011, 2013; Wang *et al.* 2018):

$$\frac{\partial}{\partial t}\left(\tfrac{1}{2}\bar{\rho}\tilde{u}_i^2\right) = -J_l - \Phi_l - \Pi_l - D_l. \tag{3.5}$$

Here J_l is the filtered spatial convection term, Φ_l is the filtered pressure dilatation term, Π_l is the SGS kinetic energy flux term and D_l is the filtered viscous dissipation term. These terms can be written as

$$J_l = \frac{\partial}{\partial x_j}\left(\tfrac{1}{2}\bar{\rho}\tilde{u}_i^2\tilde{u}_j + \bar{p}\tilde{u}_j + \bar{\rho}\tilde{\tau}_{ij}\tilde{u}_i - \frac{\tilde{u}_i\bar{\sigma}_{ij}}{Re}\right), \tag{3.6}$$

$$\Phi_l = -\bar{p}\frac{\partial \tilde{u}_i}{\partial x_i}, \tag{3.7}$$

$$\Pi_l = -\bar{\rho}\tilde{\tau}_{ij}\frac{\partial \tilde{u}_i}{\partial x_j} = -\bar{\rho}\tilde{\tau}_{ij}\tilde{S}_{ij}, \tag{3.8}$$

$$D_l = \frac{\bar{\sigma}_{ij}}{Re}\frac{\partial \tilde{u}_i}{\partial x_j} = \frac{\bar{\sigma}_{ij}\tilde{S}_{ij}}{Re}, \tag{3.9}$$

where the filtered strain-rate tensor $\tilde{S}_{ij}$ is defined as $\tilde{S}_{ij} = (1/2)(\partial\tilde{u}_i/\partial x_j + \partial\tilde{u}_j/\partial x_i)$.

To determine the properties of inter-scale transfer of kinetic energy along the wall-normal direction, the streamwise–spanwise average of the filtered kinetic energy can be written as

$$\frac{\partial}{\partial t}\left\langle \tfrac{1}{2}\bar{\rho}\tilde{u}_i^2\right\rangle_{xz} = -\langle J_l\rangle_{xz} - \langle \Phi_l\rangle_{xz} - \langle \Pi_l\rangle_{xz} - \langle D_l\rangle_{xz}. \tag{3.10}$$

Here $\langle f\rangle_{xz}$ represents the average of variable f in streamwise and spanwise directions and time.

4. Numerical results for kinetic energy transfer along wall-normal direction

The DNS is performed using the OPENCFD code, which has been widely used and validated for compressible transitional and turbulent wall-bounded flows (Li, Fu & Ma 2008; Liang & Li 2013, 2015; Zhang *et al.* 2014; She *et al.* 2018; Li *et al.* 2019; Zheng *et al.* 2019). A schematic for the spatially developing turbulent boundary layer is shown in figure 1. The boundary conditions of the hypersonic turbulent boundary layer are listed as follows: inflow and outflow boundary conditions, a wall boundary condition, an upper far-field boundary condition as well as the periodic boundary condition in the spanwise direction. To be specific, a time-independent laminar compressible boundary layer similarity solution is applied at the inflow boundary. A region of wall blowing and suction (Pirozzoli *et al.* 2004) is implemented at $4.5 \leq x \leq 5$ to lead to

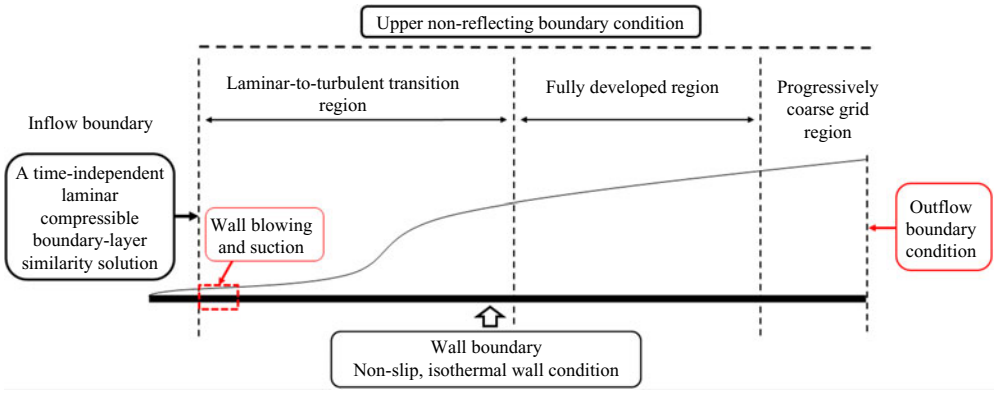

Figure 1. A schematic of the computational domain.

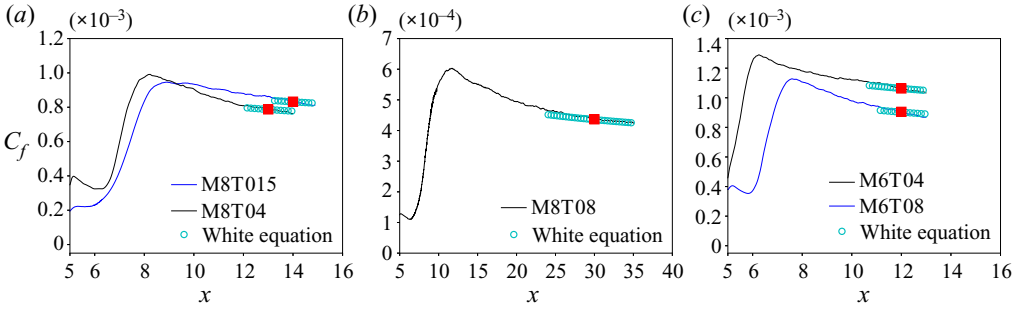

Figure 2. The skin-friction coefficient c_f along the streamwise direction x after the region of wall blowing and suction ($x > 5$). The red square represents the streamwise location x_a of the data extracted from the fully developed region of the hypersonic turbulent boundary layer. The label 'White equation' represents equation (4.1).

the laminar-to-turbulent transition. Moreover, all the flow fields are extrapolated from the interior points to the outflow boundary points except the pressure in the subsonic region of the turbulent boundary layer at the outflow condition. The pressure in the subsonic region is set equal to the value of the first grid point where the flow is supersonic. In order to prevent the reflection of disturbance due to the numerical treatment of the outflow boundary condition, a progressively coarse grid is implemented in the streamwise direction near the outflow boundary condition (Pirozzoli *et al.* 2004). Furthermore, the non-slip and isothermal conditions are applied for the wall, and the non-reflecting boundary condition is imposed for the upper boundary (Pirozzoli *et al.* 2004). The flow initially undergoes a transition in the laminar-to-turbulent transition region, and then achieves the fully developed state in the fully developed region. Progressively coarse grid is implemented in the progressively coarse grid region in figure 1.

Several hypersonic turbulent boundary layers at Mach numbers 6 and 8 with different wall temperatures are analysed numerically in the present study. The fundamental parameters of the database are listed in table 1. Here $M_\infty = U_\infty/c_\infty$ and $Re_\infty = \rho_\infty U_\infty L_\infty/\mu_\infty$ are the free-stream Mach number and Reynolds number respectively. Temperature T_w is the wall temperature and T_∞ is the free-stream temperature and considered to be $T_\infty = 169.44$ K. The recovery temperature T_r is defined as

$T_r = T_\infty(1 + r((\gamma - 1)/2)M_\infty^2)$ with recovery factor $r = 0.9$ (Duan *et al.* 2010). The computational domains L_x, L_y and L_z are non-dimensionalized by $L_\infty = 1$ inch (Pirozzoli *et al.* 2004). Directions x, y and z are the streamwise, wall-normal and spanwise directions respectively; $\Delta x^+ = \Delta x/\delta_v$ is the normalized spacing of the streamwise direction; $\Delta y_w^+ = \Delta y_w/\delta_v$ is the normalized spacing of the first point off the wall; $\Delta z^+ = \Delta z/\delta_v$ is the normalized spacing of the spanwise direction; $\delta_v = \langle\mu_w\rangle_{zt}/(\langle\rho_w\rangle_{zt}u_\tau)$ is the viscous length scale; $u_\tau = \sqrt{\tau_w/\rho_w}$ is the friction velocity; $\tau_w = (\mu(\partial\langle u\rangle_{zt}/\partial y))_{y=0}$ is the wall shear stress; ρ_w is the density on the wall; and $\langle\mu_w\rangle_{zt}$ and $\langle\rho_w\rangle_{zt}$ are the spanwise and time average of viscosity and density on the wall respectively, where $\langle f\rangle_{zt}$ represents the spanwise and time average of variable f.

The skin-friction coefficient $c_f \equiv \tau_w/(\rho_\infty U_\infty^2/2)$ along the streamwise direction x after the region of wall blowing and suction ($x > 5$) is shown in figure 2. A theoretical formula for the compressible turbulent skin friction is

$$C_f(x) = \frac{0.455}{S^2}\left[\ln\left(\frac{0.06}{S}Re_x\frac{1}{\mu_w}\sqrt{\frac{1}{T_w}}\right)\right]^{-2}, \tag{4.1}$$

with $Re_x \equiv Re_\infty x$, $S = \sqrt{T_w - 1}/\sin^{-1}A$ and $A = (r_c((\gamma - 1)/2)Ma_\infty^2(1/T_w))^{1/2}$ (White 2006; Zheng *et al.* 2019). Equation (4.1) is represented as 'White equation' shown by open circles in figure 2. It is seen that the numerical simulations show a good agreement with (4.1) in the fully developed region.

Data in a small streamwise window of $[x_a - 0.5\delta, x_a + 0.5\delta]$ extracted from the fully developed region of the hypersonic turbulent boundary layer are used for the following analysis. A number of N flow-field snapshots spanning a time interval T_f are used for analysis. The values of x_a, δ, N and T_f are listed in table 1. It is noted that the red square in figure 2 represents the streamwise location x_a of the data extracted from the hypersonic turbulent boundary layer. The streamwise location x_a is far from the transition peak and located in the fully developed region of the hypersonic turbulent boundary layer. For the computational cost, each case takes approximately T_{all} CPU hours on a 2.40 GHz Intel CPU and the values of T_{all} are listed in table 1.

It should be pointed out that the present DNS database neglects the non-equilibrium and radiative effects. The reasons are as follows. The free-stream temperature is considered to be $T_\infty = 169.44$ K. Even for the highest wall temperature case, M8T08, the greatest temperature is approximately 1700 K, where the non-equilibrium and heat radiative effects are fairly weak in this state (Anderson 2006; Duan *et al.* 2011; Lagha *et al.* 2011; Zhang *et al.* 2014; Josyula 2015; She *et al.* 2018) and can be neglected in the present simulation. Moreover, the greatest temperatures of cases 'M7', 'M8' and 'M12' in Duan *et al.* (2011) and $M_\infty = 7.5, 10, 15, 20$ in Lagha *et al.* (2011) are much larger (approximately 6400 K in 'M12' in Duan *et al.* (2011)) than that of the present case M8T08, and the non-equilibrium and heat radiative effects were also neglected in their study. It is worth noting that Zheng *et al.* (2020) concluded that vibrational relaxation has a negligible effect on the compression and expansion motions for both weakly and highly compressible turbulence with thermal non-equilibrium. The main purpose of this article is to investigate the effect of compressibility on the inter-scale transfer of kinetic energy. Accordingly, the neglect of non-equilibrium and heat radiative effects is a reasonable simplification for the present study of the hypersonic turbulent boundary layer.

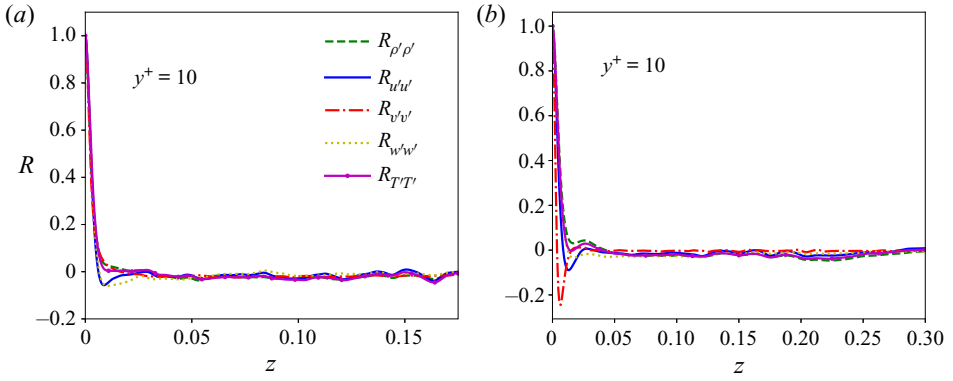

Figure 3. Distribution of the two-point correlations of fluctuating variables along the spanwise direction at $y^+ = 10$ at the streamwise location x_a in (*a*) M8T015 and (*b*) M8T08.

The two-point autocorrelation coefficient $R_{\alpha\alpha}$ can be defined as

$$R_{\alpha\alpha} = \frac{\langle \alpha(x, y, z' + z)\alpha(x, y, z')\rangle_{zt}}{\langle \alpha(x, y, z')^2\rangle_{zt}}. \tag{4.2}$$

The two-point correlations of fluctuating density, velocity and temperature of M8T015 and M8T08 at $y^+ = 10$ at the streamwise location x_a are depicted in figure 3. The x axis of figure 3 represents half the size of the spanwise domain. It is shown in figure 3 that the autocorrelations drop to nearly zero at the centre of the spanwise domain, which indicates that the present computational domain in the spanwise direction is sufficiently wide. The adequacy of the computational domain size in the spanwise direction in the other three databases is also confirmed and not shown here for brevity.

The grid resolutions of the present numerical simulations can be assessed by conducting grid convergence studies. Figure 4 shows the normalized streamwise Reynolds stress $\langle \rho u''^2\rangle_{zt}/\tau_w$ and the normalized filtered streamwise Reynolds stress $\langle \bar{\rho}\tilde{u}''^2\rangle_{zt}/\tau_w$, the normalized root-mean-square (r.m.s.) values of fluctuating temperature $\sqrt{\langle T''^2\rangle_{zt}}/T_w$ and the normalized r.m.s. values of the filtered fluctuating temperature $\sqrt{\langle \tilde{T}''^2\rangle_{zt}}/T_w$, as well as the normalized streamwise–spanwise average of the SGS flux of kinetic energy transfer at different grid resolutions listed in table 2 in M8T08. Here, the filter width is $l/\delta_v = 900$. It is found that all the curves collapse indistinguishably, indicating that the grid is fine enough for the convergence of the DNS field as well as the filtered DNS field. Grid convergence of velocity and temperature fields indicates that the present grid resolution is sufficient to resolve both the turbulent and thermal boundary layers in M8T08. Moreover, grid convergence is also examined for the SGS transfer of kinetic energy as shown in figure 4(*c*). According to the above investigations, all the curves are coincident for different resolutions, indicating that grid resolution '*A*' is sufficient to resolve the flow fields and can be used for further analysis. It is noted that the grid resolution in M8T08 is finer than that in Pirozzoli *et al.* (2004), where grid convergence was also checked in their study. The grid resolution in M8T08 is coarser than those in the other four cases. Moreover, the grid convergence was also checked in the other cases and the details are not shown here for brevity.

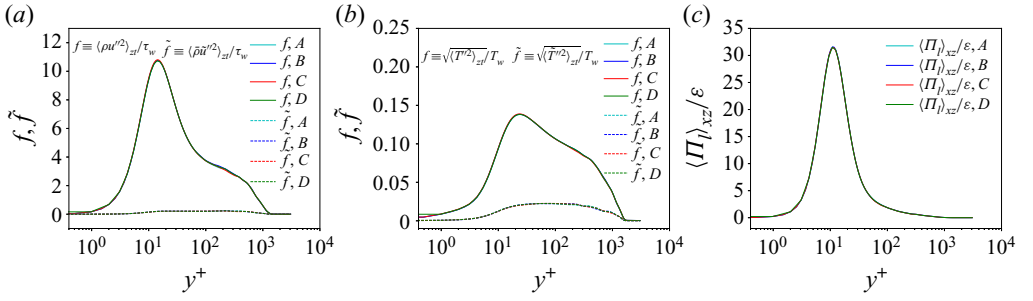

Figure 4. Grid convergence study for M8T08. (*a*) The normalized streamwise Reynolds stress $\langle \rho u''^2 \rangle_{zt}/\tau_w$ and the normalized filtered streamwise Reynolds stress $\langle \tilde{\rho}\tilde{u}''^2 \rangle_{zt}/\tau_w$ with filter width $l/\delta_v = 900$. (*b*) The normalized r.m.s. values of fluctuating temperature $\sqrt{\langle T''^2 \rangle_{zt}}/T_w$ and the normalized r.m.s. values of the filtered fluctuating temperature $\sqrt{\langle \tilde{T}''^2 \rangle_{zt}}/T_w$ with filter width $l/\delta_v = 900$. (*c*) The normalized streamwise–spanwise average of the SGS flux of kinetic energy transfer with filter width $l/\delta_v = 900$. The symbols '*A*', '*B*', '*C*' and '*D*' represent four different grid resolutions and are listed in table 2. Grid resolution '*A*' is used for further analysis.

Case	$N_x \times N_y \times N_z$	Δx^+	Δy_w^+	Δz^+
M8T08 – *A*	12 500 × 200 × 640	12.2	0.5	4.6
M8T08 – *B*	12 500 × 200 × 1280	12.2	0.5	2.3
M8T08 – *C*	25 000 × 200 × 640	6.1	0.5	4.6
M8T08 – *D*	12 500 × 100 × 640	12.2	1.0	4.6

Table 2. Four different grid resolutions used for the grid convergence studies in M8T08.

Several relevant Reynolds numbers can be defined for a compressible turbulent boundary layer. The friction Reynolds number $Re_\tau = \langle \rho_w \rangle_{zt} u_\tau \delta / \langle \mu_w \rangle_{zt}$ is defined as the ratio of the boundary layer thickness and the viscous length scale. The Reynolds number based on the momentum thickness θ_{th} and the wall viscosity, $Re_{\delta_2} = \rho_\infty u_\infty \theta_{th} / \langle \mu_w \rangle_{zt}$, is defined as the ratio of the highest momentum to the wall shear stress. Here the momentum thickness θ_{th} is defined as

$$\theta_{th} = \int_0^\delta \frac{\langle \rho \rangle_{zt} \langle u \rangle_{zt}}{\rho_\infty u_\infty} \left(1 - \frac{\langle u \rangle_{zt}}{u_\infty}\right) \mathrm{d}y, \tag{4.3}$$

where ρ_∞ and u_∞ are the free-stream density and streamwise velocity, and δ is the boundary layer thickness. Reynolds number $Re_{\theta_{th}} = \rho_\infty u_\infty \theta_{th} / \mu_\infty$ is the Reynolds number based on the momentum thickness θ_{th}. Moreover, the skin-friction coefficient c_f and wall heat flux $q_w \equiv ((\kappa/\alpha)(\partial T/\partial y))|_{y=0}$ are of great importance to both practical engineering and fundamental fluid physics in a compressible turbulent boundary layer. The above global flow properties are listed in table 3.

It has been shown that the Van Driest transformation (Van Driest 1951) can successfully make the mean velocity profiles of adiabatic compressible wall-bounded flows consistent with those of incompressible turbulence (Duan *et al.* 2011; Pirozzoli & Bernardini 2011). However, for non-adiabatic compressible wall-bounded flows, previous investigations indicate that the Van Driest transformation is no longer appropriate (Trettel & Larsson 2016; Volpiani *et al.* 2020). Better transformations for non-adiabatic wall turbulence have

Case	Re_∞	Re_τ	$Re_{\theta_{th}}$	Re_{δ_2}	c_f	q_w
M6T04	2×10^6	1615	1.12×10^4	4763	1.06×10^{-3}	1.93×10^{-4}
M6T08	2×10^6	688	9.17×10^3	2514	9.05×10^{-4}	5.11×10^{-5}
M8T015	2×10^6	2444	1.02×10^4	6018	8.32×10^{-4}	2.04×10^{-4}
M8T04	2×10^6	887	9.08×10^3	2780	7.88×10^{-4}	1.34×10^{-4}
M8T08	5×10^6	1386	3.22×10^4	6563	4.37×10^{-4}	2.46×10^{-5}

Table 3. Global flow properties for the DNS.

Transformation	f_I	g_I
Van Driest (1951)	$f_{VD} = 1$	$g_{VD} = \sqrt{R}$
Trettel & Larsson (2016)	$f_T = (\mathrm{d}/\mathrm{d}y)(yR^{1/2}/M)$	$g_T = M(\mathrm{d}/\mathrm{d}y)(yR^{1/2}/M)$
Volpiani *et al.* (2020)	$f_V = \sqrt{R/M^3}$	$g_V = \sqrt{R/M}$

Table 4. Expressions of f_I and g_I for various transformations in (4.4*a*,*b*), where $R = \langle\rho\rangle_{zt}/\rho_w$ and $M = \langle\mu\rangle_{zt}/\mu_w$.

been widely investigated, which can be expressed in a general form (Modesti & Pirozzoli 2016) as

$$y_I = \int_0^y f_I \,\mathrm{d}y, \quad u_I = \int_0^u g_I \,\mathrm{d}u, \tag{4.4a,b}$$

where y_I and u_I represent the 'incompressible' values obtained from different transformations. Three typical transformations are listed in table 4, namely the transformations of Van Driest (1951), Trettel & Larsson (2016) and Volpiani *et al.* (2020). Mean velocity profiles with the three transformations are shown in figure 5. It is found that the Van Driest transformation (Van Driest 1951) shows the worst results, and obeys neither the linear law in the viscous sublayer nor the log law in the logarithmic region as in incompressible wall-bounded flows. This observation is consistent with previous reports in the cases with strong wall temperature gradient (Duan *et al.* 2010; Trettel & Larsson 2016). The transformation of Trettel & Larsson (2016) is derived based on the mean momentum equation, and obeys the linear law in the viscous sublayer. However, a deviation from the standard log law ($u^+ = (1/\kappa)\ln y^+ + C$) of the incompressible turbulent channel flows is observed for the transformation of Trettel & Larsson (2016). The above findings are consistent with previous observations in hypersonic turbulent boundary layers with cold wall condition (Zhang, Duan & Choudhari 2018; Volpiani *et al.* 2020). The transformation of Volpiani *et al.* (2020) enforces the universality of the viscous sublayer and Morkovin-scaled shear stress, and then determines the free parameters with a data-driven method to make the mean velocity profiles of the hypersonic turbulent boundary layer consistent with the same log law as that of the incompressible wall-bounded flows. It is found that the transformation of Volpiani *et al.* (2020) gives the best results, and obeys both the linear law and log law as in incompressible wall-bounded flows.

The r.m.s. values of the normalized dilatation fluctuation $\langle(\theta''^+)^2\rangle_{zt}^{1/2}$ along the wall-normal direction are plotted in figure 6(*a*). It is found that the case with a higher Mach number and a lower wall temperature results in a much larger r.m.s. value of the

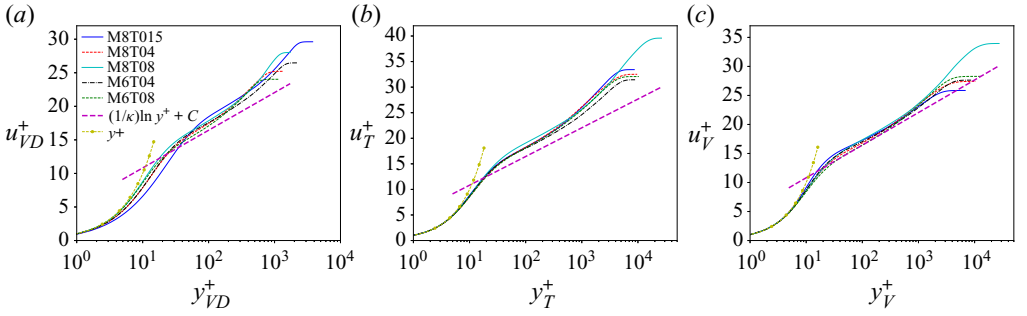

Figure 5. Mean velocity profiles with the transformations of (*a*) Van Driest (1951), (*b*) Trettel & Larsson (2016) and (*c*) Volpiani *et al.* (2020), as defined in table 4. Here $\kappa \approx 0.41$ and $C \approx 5.2$, which refer to the incompressible turbulent channel flows (Bradshaw 1977).

normalized dilatation fluctuation $\langle(\theta''^{+})^2\rangle_{zt}^{1/2}$, which indicates a stronger compressibility effect in the near-wall region. Accordingly, it is observed that a colder wall temperature gives rise to a higher compressibility near the wall, which is consistent with previous observations of Duan *et al.* (2010) and Zhang *et al.* (2018). The intrinsic rationale can be explained as follows. The colder wall temperature results in a stronger temperature gradient near the wall, and the stronger temperature gradient leads to a stronger wall heat flux q_w (listed in table 3). It is shown in table 3 that the colder wall temperature case has a larger wall heat flux q_w, which further results in a stronger compressibility effect near the wall.

Instantaneous fields of the normalized dilatation fluctuation θ''^{+} in a wall-parallel plane at $y^+ = 10$ are shown in figure 6(*b–f*). Specifically, negative and positive θ''^{+} values form spatial spots that are well arranged as wavelike alternating patterns along the streamwise direction. The case with a higher Mach number and a lower wall temperature (particularly M8T015) exhibits much more intense alternating positive and negative structures of θ''^{+}, indicating a stronger compressibility. Moreover, the alternating positive and negative structures of θ''^{+} are consistent with the behaviour of the dilatational velocities, which exhibit spanwise ripples travelling like streamwise wave packets from left to right shown by the instantaneous fields of the dilatational velocities in Xu *et al.* (2021). The instantaneous fields of streamwise and vertical velocities as well as their solenoidal and dilatational components at $y^+ = 10$ are shown in Xu *et al.* (2021).

The Lamb vector acts as a vortex force, while the Lamb vector divergence represents the dynamical mechanisms of the momentum and vorticity transport and captures the self-sustaining interactions between coherent motions in a flow field (Hamman, Klewicki & Kirby 2008; Chen, Xu & Lu 2010). The Lamb vector is defined as $\boldsymbol{L} \equiv \boldsymbol{\omega} \times \boldsymbol{u}$. The solenoidal and dilatational components of the Lamb vector are $\boldsymbol{L}_s \equiv \boldsymbol{\omega} \times \boldsymbol{u}_s$ and $\boldsymbol{L}_d \equiv \boldsymbol{\omega} \times \boldsymbol{u}_d$ respectively. Therefore, the Lamb vector divergence and its solenoidal and dilatational components are

$$\nabla \cdot \boldsymbol{L} = \boldsymbol{u} \cdot \nabla \times \boldsymbol{\omega} - \boldsymbol{\omega} \cdot \boldsymbol{\omega}, \tag{4.5}$$

$$\nabla \cdot \boldsymbol{L}_s = \boldsymbol{u}_s \cdot \nabla \times \boldsymbol{\omega} - \boldsymbol{\omega} \cdot \boldsymbol{\omega}, \tag{4.6}$$

$$\nabla \cdot \boldsymbol{L}_d = \boldsymbol{u}_d \cdot \nabla \times \boldsymbol{\omega}. \tag{4.7}$$

The solenoidal components are similar to the incompressible Lamb vector and Lamb vector divergence, while the dilatational components are due to the compressible effect. The instantaneous fields of the Lamb vector divergence and its solenoidal and dilatational

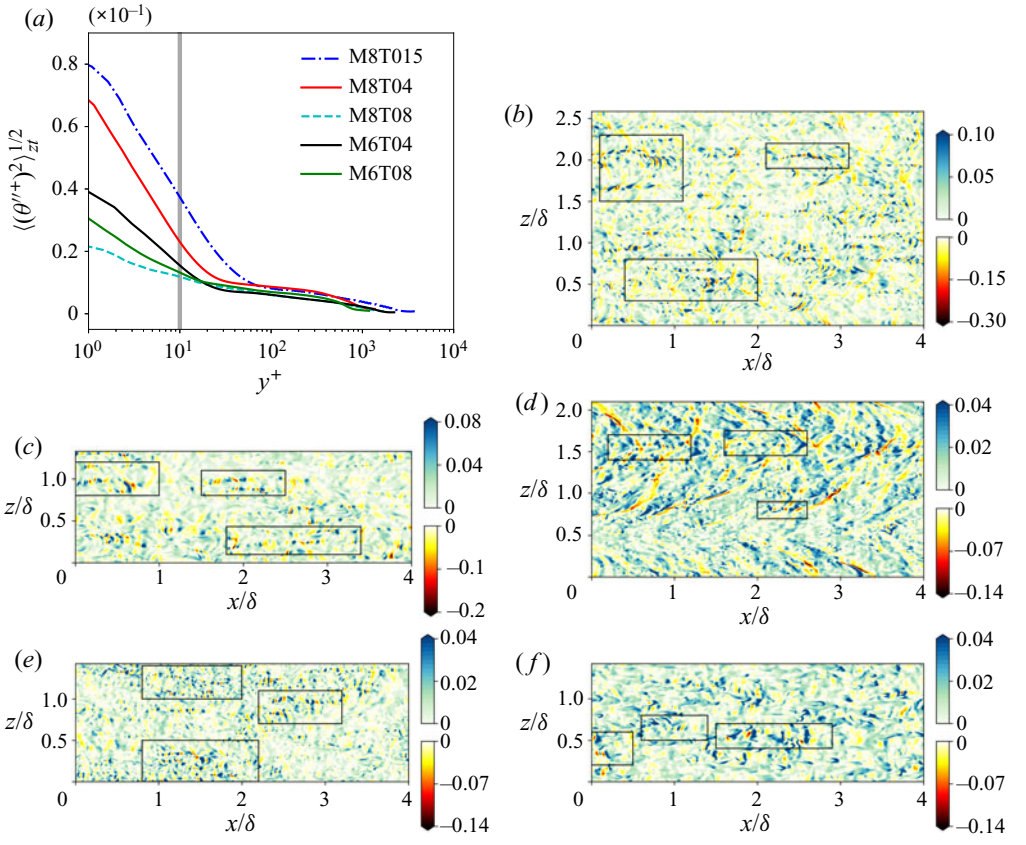

Figure 6. (*a*) The r.m.s. values of the normalized dilatation fluctuation $\langle(\theta''^+)^2\rangle_{zt}^{1/2}$ along the wall-normal direction. Here $\theta'' \equiv \partial u_k''/\partial x_k$ is the dilatation fluctuation. The grey vertical line represents the wall-normal location $y^+ = 10$. Instantaneous fields of the normalized dilatation fluctuation θ''^+ in a wall-parallel plane at $y^+ = 10$ in (*b*) M8T015, (*c*) M8T04, (*d*) M8T08, (*e*) M6T04 and (*f*) M6T08. Some typical alternating positive and negative patterns have been highlighted with black rectangles.

components in a wall-parallel plane at $y^+ = 10$ in M8T015 are shown in figure 7. Based on the analysis of the Lamb vector divergence (Hamman *et al.* 2008), the negative and positive values represent vorticity-bearing motions and straining motions respectively. It is shown in figure 7(*a*) that most of regions are occupied by the negative values of the Lamb vector divergence, indicating that the vorticity-bearing motions are dominant in the flow field. The strong positive values are always accompanied by strong negative values, indicating that the interaction between the strong straining motions and the strong vorticity-bearing motions undergoes a momentum exchange (Hamman *et al.* 2008). Moreover, the instantaneous field of $\boldsymbol{\nabla}\cdot\boldsymbol{L}_s$ is similar to that of $\boldsymbol{\nabla}\cdot\boldsymbol{L}$, implying that the solenoidal component plays a dominant role in the Lamb vector divergence. The dilatational component is much smaller than the solenoidal component, and exhibits special alternating positive and negative structures, which are consistent with the behaviour of θ''^+ shown in figure 6(*b–f*). It is noted that the Lamb vector divergence appears as an acoustic source term in Lighthill's wave equation (Lighthill 1952; Howe 1975). Accordingly, the negative and positive structures of $\boldsymbol{\nabla}\cdot\boldsymbol{L}_d$ arranged as wavelike alternating patterns are consistent with the acoustic character.

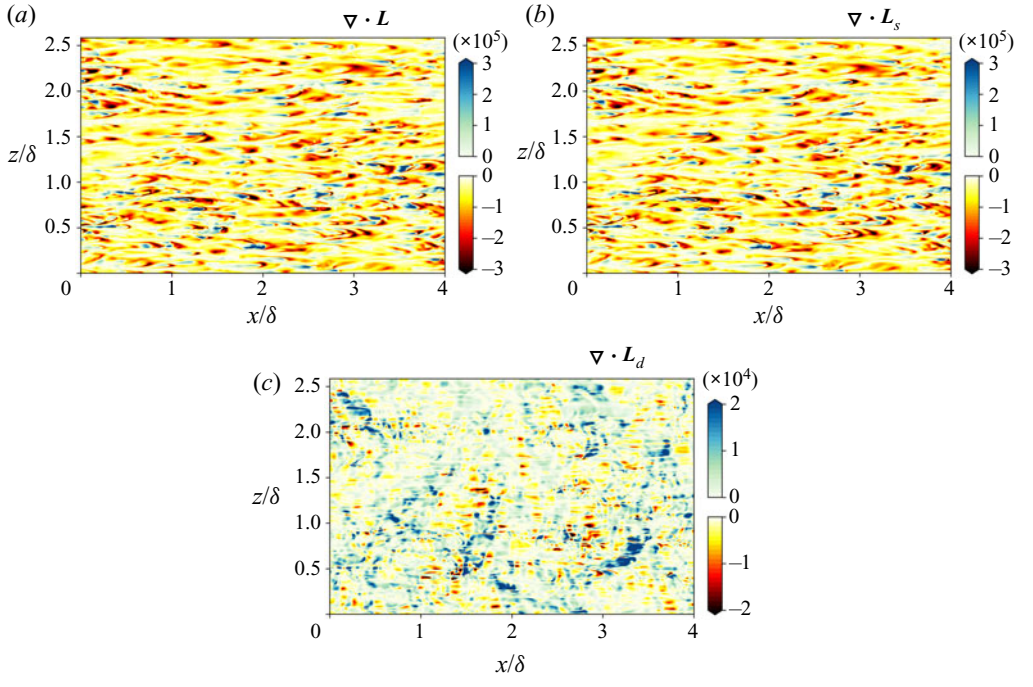

Figure 7. The instantaneous fields of (*a*) the Lamb vector divergence and its (*b*) solenoidal and (*c*) dilatational components in a wall-parallel plane at $y^+ = 10$ in M8T015.

In this section, we investigate the inter-scale transfer of kinetic energy along the wall-normal direction in a hypersonic turbulent boundary layer. The effects of wall temperature as well as local compressibility on the SGS kinetic energy flux are discussed.

4.1. *Statistics of kinetic energy transfer across scales along wall-normal direction*

Figure 8 depicts the normalized streamwise–spanwise averages of inter-scale kinetic energy transfer terms of (3.6)–(3.9) along the wall-normal direction at filter widths $l/\delta_v = 15$ and 900 in M8T015 and M8T08. It is shown that the filtered pressure dilatation term $\langle \Phi_l \rangle_{xz}/\varepsilon$ is negligibly small along the wall-normal direction, while the filtered spatial convection term $\langle J_l \rangle_{xz}/\varepsilon$ and filtered viscous dissipation term $\langle D_l \rangle_{xz}/\varepsilon$ are dominant in the near-wall region and decrease rapidly away from wall. The SGS flux term $\langle \Pi_l \rangle_{xz}/\varepsilon$ achieves its peak value in the buffer layer at large filter width $l/\delta_v = 900$.

The normalized streamwise–spanwise averages of inter-scale kinetic energy transfer terms of (3.6)–(3.9) along the wall-normal direction at different filter widths in M8T015 are shown in figure 9. It is shown that the normalized streamwise–spanwise averages of inter-scale kinetic energy transfer terms along the wall-normal direction are coincident for different filter widths at large scales. The behaviours of inter-scale kinetic energy transfer terms at different filter widths are qualitatively consistent with the energy-cascade hypothesis in the statistical sense: kinetic energy is generated at large scales, transferred gradually to smaller scales and finally dissipated by viscosity at small scales. The filtered viscous dissipation term $\langle D_l \rangle_{xz}/\varepsilon$ decays rapidly as the filter width l/δ_v increases, indicating that the kinetic energy is dissipated by viscosity at the Kolmogorov scale and is

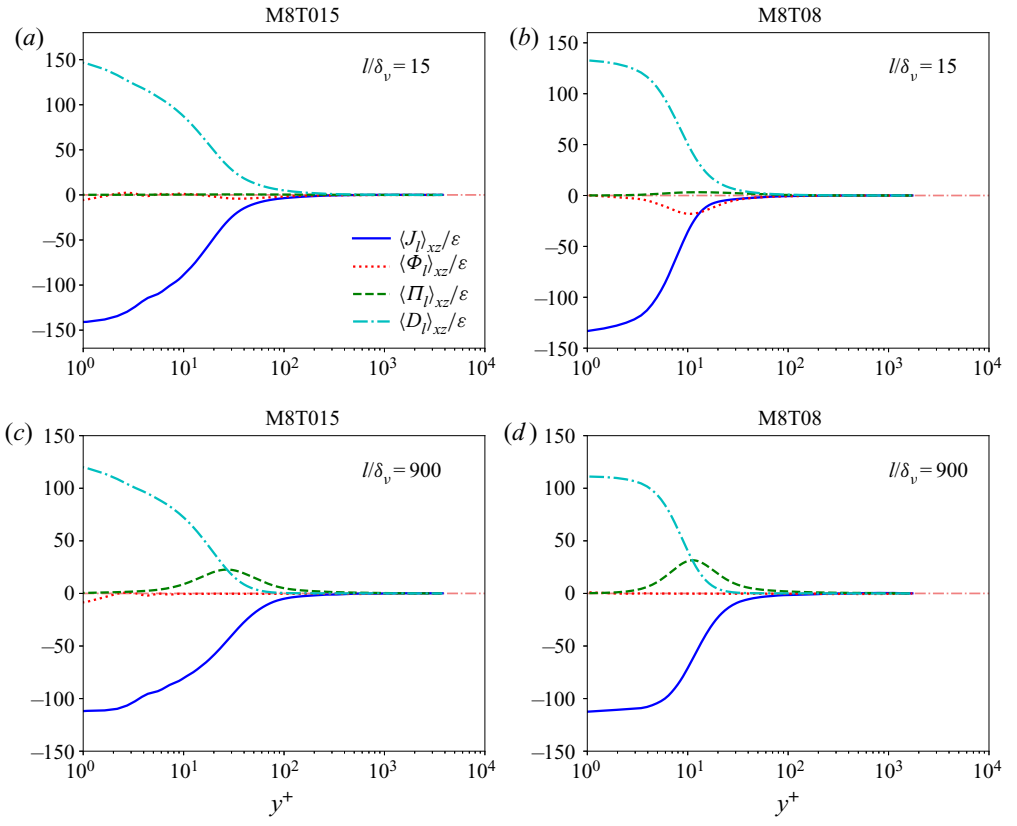

Figure 8. The normalized streamwise–spanwise averages of inter-scale kinetic energy transfer terms of (3.6)–(3.9) along the wall-normal direction at filter widths $l/\delta_v = 15$ and 900 in M8T015 and M8T08. All the inter-scale kinetic energy transfer terms are normalized by the viscous dissipation $\varepsilon \equiv \langle D\rangle$.

consistent with previous theoretical (Aluie 2011, 2013) and numerical (Wang *et al.* 2018) analyses of the filtered viscous dissipation in isotropic compressible flows. However, the filtered viscous dissipation $\langle D_l\rangle_{xz}/\varepsilon$ cannot decay to zero at large scales near the wall, which will be explained later. The SGS flux $\langle \Pi_l\rangle_{xz}/\varepsilon$ increases from zero as the filter width l/δ_v increases from the Kolmogorov scale to the inertial range. Moreover, the average values of the SGS flux $\langle \Pi_l\rangle_{xz}/\varepsilon$ along the wall-normal direction at large filter widths are coincident for different filter widths, which implies the nearly statistically invariant property of kinetic energy transfer across scales in the inertial range. Accordingly, the inertial range is nearly $l/\delta_v = 900$–1350. It is also worth noting that the filtered spatial convection term $\langle J_l\rangle_{xz}/\varepsilon$ is dominant in the near-wall region even at the largest filter width $l/\delta_v = 1350$. Moreover, the filtered pressure dilatation $\langle \Phi_l\rangle/\varepsilon$ decays to almost zero quickly in the buffer layer as the scale l/δ_v increases, indicating that the net contribution of pressure dilatation to the average kinetic energy is negligibly small at large scales. Similar observations have also been reported for previous studies of isotropic compressible turbulence (Aluie *et al.* 2012; Wang *et al.* 2012*a*, 2018; Jagannathan & Donzis 2016).

It has been noted that the filtered viscous dissipation $\langle D_l\rangle_{xz}/\varepsilon$ cannot decay to zero at large scales near the wall. The values of $\langle D_l\rangle_{xz}/\varepsilon$ along with different filter widths at $y^+ = 10$, 20, 50 and 100 in M8T015 are shown in figure 10(*a*). It is found that $\langle D_l\rangle_{xz}/\varepsilon$ cannot decay to zero at large scales in the near-wall region, while at the far-wall region

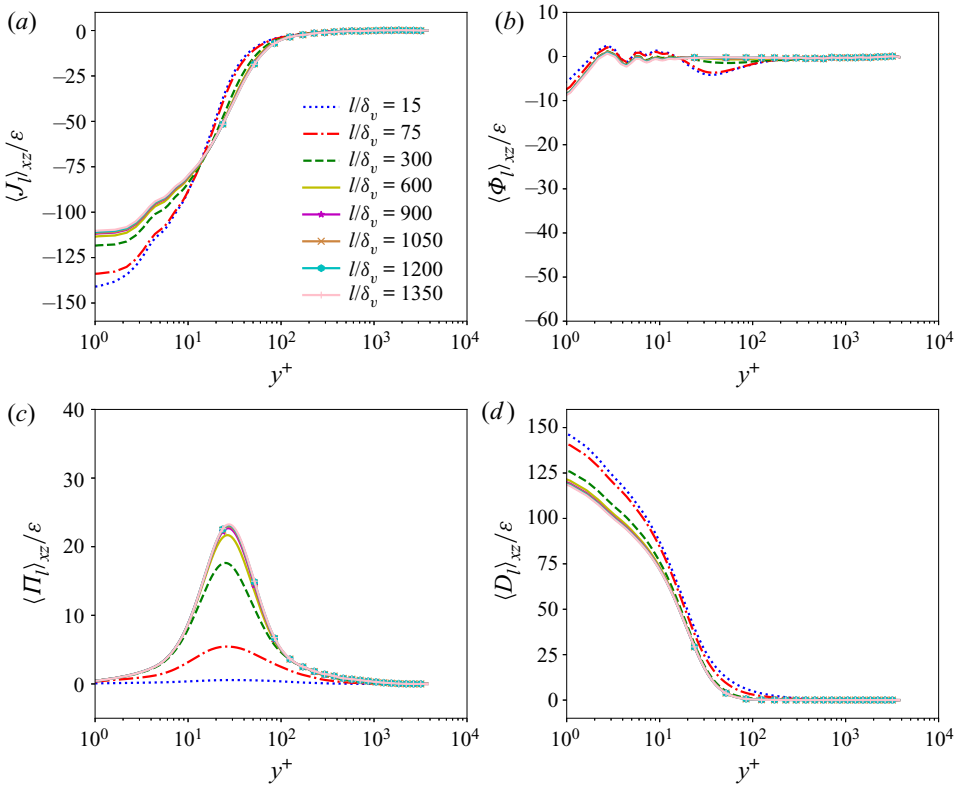

Figure 9. The normalized streamwise–spanwise averages of inter-scale kinetic energy transfer terms of (3.6)–(3.9) along the wall-normal direction at different filter widths in M8T015.

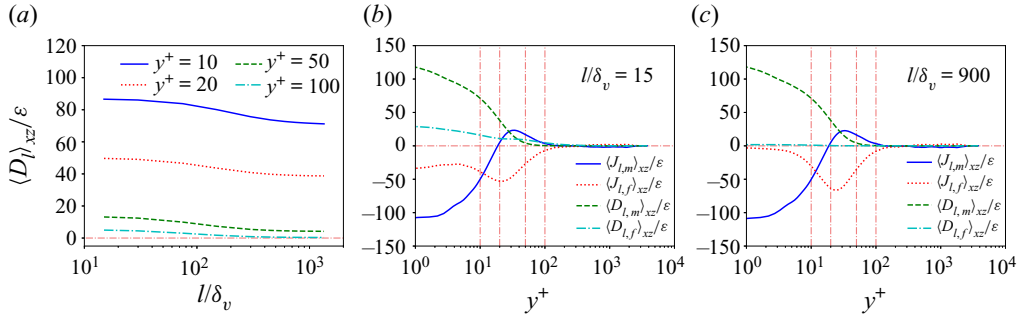

Figure 10. (*a*) The values of $\langle D_l\rangle_{xz}/\varepsilon$ along with different filter widths at $y^+ = 10$, 20, 50 and 100 in M8T015. The normalized streamwise–spanwise averages of $J_{l,m}$, $J_{l,f}$, $D_{l,m}$ and $D_{l,f}$ along the wall-normal direction at filter widths (*b*) $l/\delta_v = 15$ and (*c*) 900 in M8T015. The vertical dash-dotted lines from left to right represent position $y^+ = 10$, 20, 50 and 100, respectively.

($y^+ = 100$), $\langle D_l\rangle_{xz}/\varepsilon$ decays to almost zero in the inertial range, which is the same as the results for compressible isotropic turbulence (Wang *et al.* 2018).

The above observations can be explained as follows. A simple decomposition is applied to identify the influence of the mean flow velocities $(u_i)_{fa}$ (Favre average of velocities u_i),

which is expressed as follows:

$$J_l = J_{l,m} + J_{l,f}, \tag{4.8}$$

$$D_l = D_{l,m} + D_{l,f}, \tag{4.9}$$

where $J_{l,m}$ and $D_{l,m}$ are the filtered spatial convection term and filtered viscous dissipation term based on the mean flow velocities $(u_i)_{fa}$, while $J_{l,f}$ and $D_{l,f}$ are the filtered spatial convection term and filtered viscous dissipation term resulting from the interaction between mean flow velocities $(u_i)_{fa}$ and fluctuating velocities u_i'', as well as the interaction among the fluctuating velocities u_i''. These terms can be written as

$$J_{l,m} = \frac{\partial}{\partial x_j}\left(\frac{1}{2}\bar{\rho}\widetilde{(u_i)_{fa}}^2\widetilde{(u_j)_{fa}} + \bar{p}\widetilde{(u_j)_{fa}} + \bar{\rho}\widetilde{(\tau_{ij})_{fa}}\widetilde{(u_i)_{fa}} - \frac{\widetilde{(u_i)_{fa}}\,\overline{(\sigma_{ij})_{ra}}}{Re}\right), \tag{4.10}$$

$$J_{l,f} = J_l - J_{l,m}, \tag{4.11}$$

$$D_{l,m} = \frac{\overline{(\sigma_{ij})_{ra}}}{Re}\frac{\partial\widetilde{(u_i)_{fa}}}{\partial x_j} = \frac{\overline{(\sigma_{ij})_{ra}}\,\widetilde{(S_{ij})_{fa}}}{Re}, \tag{4.12}$$

$$D_{l,f} = D_l - D_{l,m}. \tag{4.13}$$

Here $(\sigma_{ij})_{ra}$ is the Reynolds average of viscous stress σ_{ij}, $\widetilde{(\tau_{ij})_{fa}}$ and $(S_{ij})_{fa}$ are the mean SGS stress and the mean strain-rate tensor calculated by the mean velocities $(u_i)_{fa}$, which are defined as

$$\widetilde{(\tau_{ij})_{fa}} = \widetilde{(u_i)_{fa}(u_j)_{fa}} - \widetilde{(u_i)_{fa}}\,\widetilde{(u_j)_{fa}}, \tag{4.14}$$

$$(S_{ij})_{fa} = \frac{1}{2}\left(\frac{\partial(u_i)_{fa}}{\partial x_j} + \frac{\partial(u_j)_{fa}}{\partial x_i}\right). \tag{4.15}$$

The normalized streamwise–spanwise averages of $J_{l,m}$, $J_{l,f}$, $D_{l,m}$ and $D_{l,f}$ along the wall-normal direction at filter widths $l/\delta_\nu = 15$ and 900 in M8T015 are depicted in figures 10(*b*) and 10(*c*). It is found that at small filter width $l/\delta_\nu = 15$, $\langle D_{l,m}\rangle_{xz}/\varepsilon$ and $\langle D_{l,f}\rangle_{xz}/\varepsilon$ exhibit their peak values near the wall and drop quickly away from the wall. Moreover, $\langle D_{l,f}\rangle_{xz}/\varepsilon \ll \langle D_{l,m}\rangle_{xz}/\varepsilon$. As the filter width increases to the inertial range ($l/\delta_\nu = 900$), $\langle D_{l,f}\rangle_{xz}/\varepsilon$ decays to almost zero along the wall-normal direction, while $\langle D_{l,m}\rangle_{xz}/\varepsilon$ is nearly unchanged along the wall-normal direction. Accordingly, the non-zero $\langle D_l\rangle_{xz}/\varepsilon$ in the near-wall region at large filter width is mainly due to the mean filtered viscous dissipation term $\langle D_{l,m}\rangle_{xz}/\varepsilon$. At the far-wall region (such as $y^+ = 100$ in figure 10*a*), $\langle D_{l,m}\rangle_{xz}/\varepsilon$ decays to almost zero, which results in the negligibly small $\langle D_l\rangle_{xz}/\varepsilon$ at large scales.

It is shown that $\langle J_{l,m}\rangle_{xz}/\varepsilon$ achieves its peak value near the wall, which results in the domination of the filtered spatial convection term $\langle J_l\rangle_{xz}/\varepsilon$ in the near-wall region; $\langle J_{l,f}\rangle_{xz}/\varepsilon$ attains its peak value in the buffer layer. As filter width increases, $\langle J_{l,m}\rangle_{xz}/\varepsilon$ is nearly unchanged along the wall-normal direction, while the magnitude of $\langle J_{l,f}\rangle_{xz}/\varepsilon$ decreases near the wall, and increases in the buffer layer.

An interesting phenomenon is found that the wall temperature has a significant influence on the kinetic energy transfer, especially on the filtered pressure dilatation term Φ_l and the SGS flux term Π_l. The normalized streamwise–spanwise average of the filtered pressure dilatation $\langle\Phi_l\rangle_{xz}/\varepsilon$ and the r.m.s. values of the filtered pressure dilatation $\Phi_{l,rms}/\varepsilon$ along the wall-normal direction at filter widths $l/\delta_\nu = 15$, 300 and 900 in M8T015 and M8T08

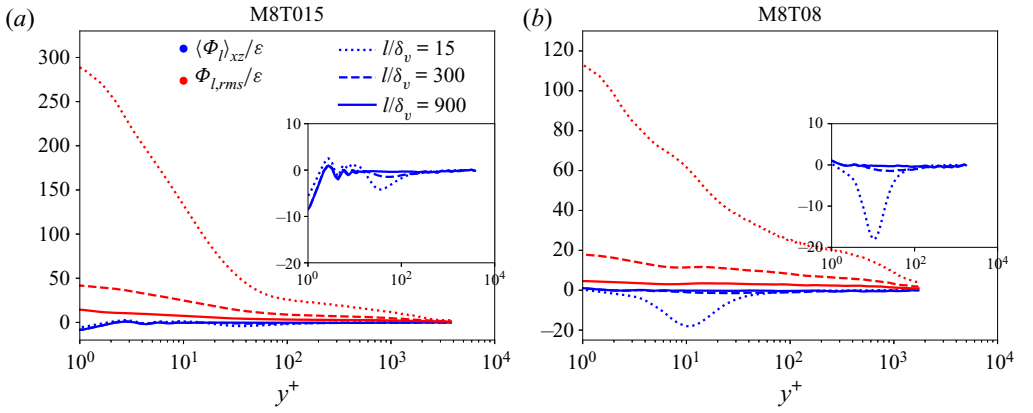

Figure 11. The normalized streamwise–spanwise average of the filtered pressure dilatation $\langle\Phi_l\rangle_{xz}/\varepsilon$ and the r.m.s. values of the filtered pressure dilatation $\Phi_{l,rms}/\varepsilon$ along the wall-normal direction at filter widths $l/\delta_v =$ 15, 300 and 900 in (*a*) M8T015 and (*b*) M8T08.

are shown in figure 11. The r.m.s. value of the filtered pressure dilatation $\Phi_{l,rms}$ is defined as $\Phi_{l,rms} = \sqrt{\langle(\Phi_l)^2\rangle_{xz}}$. It is shown that $\langle\Phi_l\rangle_{xz}/\varepsilon$ and $\Phi_{l,rms}/\varepsilon$ decrease quickly as filter width increases, indicating that the net contribution of pressure dilatation to the average kinetic energy is prominent only at small scales, and the pressure dilatation has a significant effect on the local conversion between kinetic energy and internal energy. The fact that $\Phi_{l,rms}/\varepsilon \gg \langle\Phi_l\rangle_{xz}/\varepsilon$ indicates the significant cancellation between positive and negative values of filtered pressure dilatation. Moreover, $\Phi_{l,rms}/\varepsilon$ attains its peak value near the wall, and is much larger in M8T015 than in M8T08, which indicates that the cold wall temperature induces a much stronger compressibility in the near-wall region.

The probability density function (PDF) of the normalized SGS flux Π_l/ε along the wall-normal direction in the inertial range $l/\delta_v = 900$ is shown in figure 12(*a–e*). It is found that the negative values of the normalized SGS flux Π_l/ε appear in some flow regions as indicated by the negative side of the PDF, especially in M8T015. The negative value of SGS flux can be interpreted as the SGS backscatter of kinetic energy, i.e. the reverse transfer of kinetic energy from small scales to large scales. The PDF of the SGS flux exhibits a strong positive skewness in the inertial range, especially in M6T04, M6T08, M8T04 and M8T08, where almost all values of the SGS flux are larger than zero. It is also found that the degree of the positive skewness becomes weaker as the wall temperature decreases, indicating that the cold wall temperature enhances the local reverse transfer of kinetic energy from small scales to large scales. The above observation indicates that the kinetic energy transfer has a tendency to be from large scales to small scales, and the cold wall temperature suppresses this local direct transfer of kinetic energy. The PDF of the normalized SGS flux Π_l/ε at $y^+ = 10$ at different filter widths in M8T015 and M8T08 is depicted in figure 12(*f*,*g*). It is illustrated that local reverse transfer of kinetic energy appears frequently at small scales. As filter width increases, local reverse transfer of kinetic energy is markedly suppressed. It is also found that the peak values of the PDF of the SGS flux increase as filter width increases, indicating that more positive SGS flux appears at large scales. The two tails of the PDF of the SGS flux become longer as filter width decreases, due to the fact that local energy transfer is more intermittent at small scales than at large scales. The differences of PDFs in M8T015 and M8T08 are more significant at small scales than

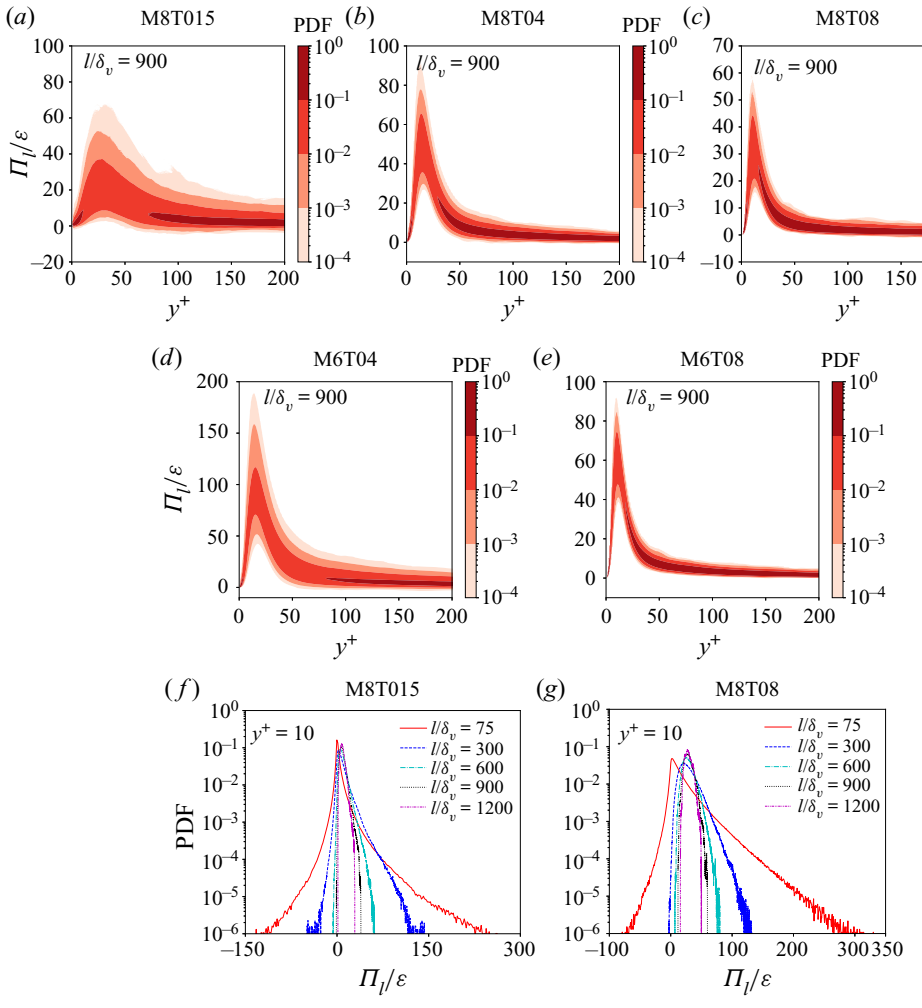

Figure 12. The PDF of the normalized SGS flux Π_l/ε along the wall-normal direction in the inertial range $l/\delta_v = 900$ in (*a*) M8T015, (*b*) M8T04, (*c*) M8T08, (*d*) M6T04 and (*e*) M6T08. The PDF of the normalized SGS flux Π_l/ε at $y^+ = 10$ at different filter widths in (*f*) M8T015 and (*g*) M8T08.

at large scales, implying that the effect of wall temperature is more prominent at small scales.

4.2. *Effect of fluctuating velocity divergence on SGS flux of kinetic energy*

The filtered fluctuating velocity divergence is denoted by $\theta_l'' = \partial \tilde{u}_i''/\partial x_i$, representing the strength of local compression and expansion motions. Figure 13 shows the conditional streamwise–spanwise average of normalized SGS flux $\langle \Pi_l/\varepsilon \mid \theta_l''^+ \rangle_{xz}$ along the wall-normal direction in the inertial range $l/\delta_v = 900$ in M8T015 and M8T08. It is found that $\langle \Pi_l/\varepsilon \mid \theta_l''^+ \rangle_{xz}$ is positive almost everywhere, except for some strong expansion regions in M8T015, indicating that the direct transfer of kinetic energy from large scales to small scales is dominant in the hypersonic turbulent boundary layer. It is also found

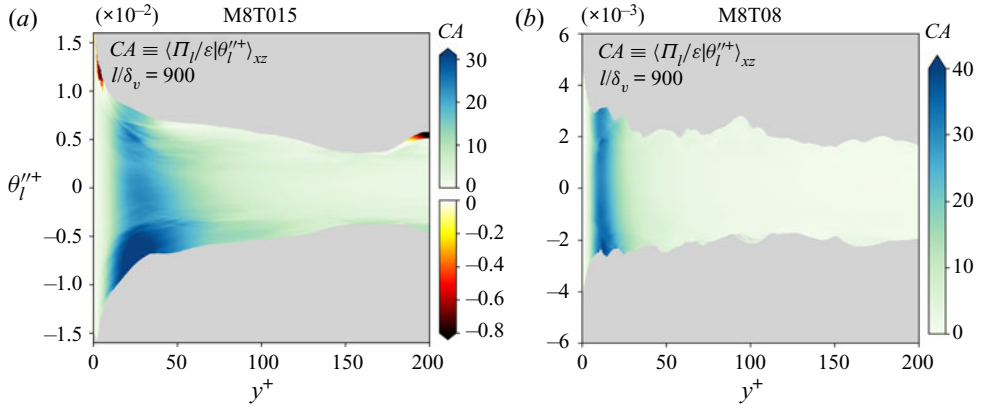

Figure 13. The streamwise–spanwise average of the normalized SGS flux Π_l/ε conditioned on the normalized filtered fluctuating velocity divergence $\theta_l''^+$ along the wall-normal direction at filter width $l/\delta_v = 900$ in (*a*) M8T015 and (*b*) M8T08.

that $\langle \Pi_l/\varepsilon \mid \theta_l''^+ \rangle_{xz}$ decreases as the normalized filtered fluctuating velocity divergence $\theta_l''^+$ increases from negative to positive, indicating that the local reverse transfer of kinetic energy is mainly concentrated in the expansion region. Wall temperature has a significant effect on $\langle \Pi_l/\varepsilon \mid \theta_l''^+ \rangle_{xz}$. It is shown that negative values of $\langle \Pi_l/\varepsilon \mid \theta_l''^+ \rangle_{xz}$ appear in some strong expansion regions in M8T015, and the values of $\langle \Pi_l/\varepsilon \mid \theta_l''^+ \rangle_{xz}$ in M8T015 are smaller than those in M8T08, indicating that the cold wall temperature enhances the reverse transfer of kinetic energy.

A variable β_l is introduced to investigate the relation between the filtered strain-rate tensor and the SGS stress, which is defined as (Wang *et al.* 2018)

$$\beta_l = \frac{\tilde{\tau}_{ij}\tilde{S}_{ij}}{|\tilde{\tau}||\tilde{S}|}, \tag{4.16}$$

where $|\tilde{\tau}| = \sqrt{\tilde{\tau}_{ij}\tilde{\tau}_{ij}}$ and $|\tilde{S}| = \sqrt{\tilde{S}_{ij}\tilde{S}_{ij}}$. Figure 14 shows the streamwise–spanwise average of β_l conditioned on the normalized filtered fluctuating velocity divergence $\theta_l''^+$ along the wall-normal direction at filter width $l/\delta_v = 900$ in M8T015 and M8T08. A negative $\langle \beta_l \mid \theta_l''^+ \rangle_{xz}$ represents the direct transfer of kinetic energy from large scales to small scales, while a positive $\langle \beta_l \mid \theta_l''^+ \rangle_{xz}$ represents the reverse transfer of kinetic energy from small scales to large scales (Wang *et al.* 2018). It is shown that $\langle \beta_l \mid \theta_l''^+ \rangle_{xz}$ is almost zero near the wall, implying the nearly perpendicular relation between the filtered strain-rate tensor and the SGS stress in the near-wall region. As wall-normal distance increases, the magnitudes of $\langle \beta_l \mid \theta_l''^+ \rangle_{xz}$ increase, demonstrating the high efficiency of inter-scale kinetic energy transfer far from the wall. Accordingly, the wall suppresses the efficiency of the inter-scale kinetic energy transfer. Moreover, $\langle \beta_l \mid \theta_l''^+ \rangle_{xz}$ exhibits more negative values in strong compression regions, demonstrating the higher efficiency of direct inter-scale kinetic energy transfer induced by compression motions. The magnitude of $\langle \beta_l \mid \theta_l''^+ \rangle_{xz}$ is smaller in M8T015 than in M8T08, indicating that the cold wall temperature weakens the efficiency of the inter-scale kinetic energy transfer.

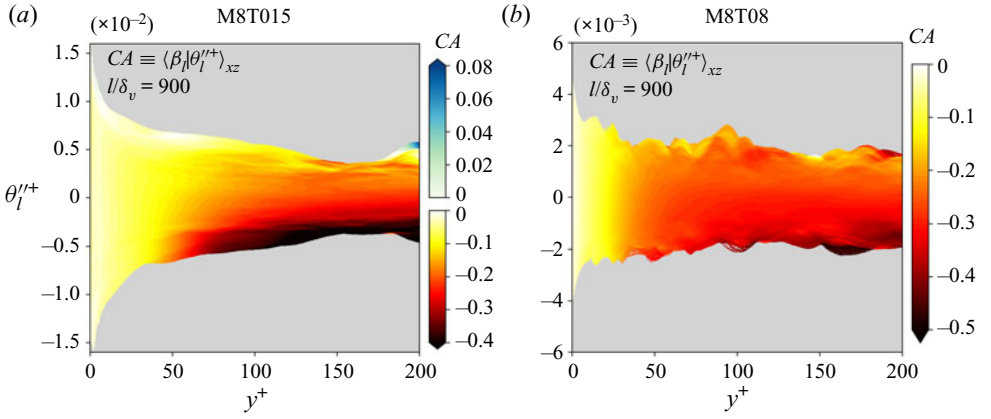

Figure 14. The streamwise–spanwise average of β_l conditioned on the normalized filtered fluctuating velocity divergence $\theta_l''^{+}$ along the wall-normal direction at filter width $l/\delta_v = 900$ in (*a*) M8T015 and (*b*) M8T08.

5. Mean-fluctuating decomposition and Helmholtz decomposition on SGS flux of kinetic energy

In this section, mean-fluctuating decomposition is applied to identify the influence of mean flow velocities. Moreover, Helmholtz decomposition of the velocity fields is also introduced to explore the compressibility effect in an isothermal hypersonic turbulent boundary layer.

The velocity field can be divided into $\boldsymbol{u} = (\boldsymbol{u})_{fa} + \boldsymbol{u}''$. Furthermore, the fluctuating velocities $\boldsymbol{u}''$ can be decomposed into a solenoidal ($\boldsymbol{u}_s''$) and a dilatational ($\boldsymbol{u}_d''$) component.

Accordingly, the SGS stress $\bar{\rho}\tilde{\tau}_{ij}$ can be divided into

$$\bar{\rho}\tilde{\tau}_{ij} = \tilde{\tau}_{m,ij} + \tilde{\tau}_{f,ij} + \tilde{\tau}_{in,ij}, \tag{5.1}$$

where $\tilde{\tau}_{m,ij}$ is the mean SGS stress term based on the mean velocities $(\boldsymbol{u})_{fa}$, $\tilde{\tau}_{f,ij}$ is the fluctuating SGS stress resulting from the fluctuating velocities $\boldsymbol{u}''$ and $\tilde{\tau}_{in,ij}$ is the SGS stress due to the interaction between the mean velocities $(\boldsymbol{u})_{fa}$ and fluctuating velocities $\boldsymbol{u}''$. These terms can be written as

$$\tilde{\tau}_{m,ij} \equiv \bar{\rho}(\widetilde{(u_i)_{fa}(u_j)_{fa}} - \widetilde{(u_i)_{fa}}\,\widetilde{(u_j)_{fa}}), \tag{5.2}$$

$$\tilde{\tau}_{f,ij} \equiv \bar{\rho}(\widetilde{u_i''u_j''} - \widetilde{u_i''}\,\widetilde{u_j''}), \tag{5.3}$$

$$\tilde{\tau}_{in,ij} \equiv \bar{\rho}\tilde{\tau}_{ij} - \tilde{\tau}_{m,ij} - \tilde{\tau}_{f,ij}. \tag{5.4}$$

Therefore, the SGS flux of kinetic energy Π_l can be decomposed by

$$\begin{aligned}\Pi_l &= -\tilde{\tau}_{m,ij}\widetilde{(S_{ij})_{fa}} - \tilde{\tau}_{m,ij}\widetilde{S}_{ij}'' - \tilde{\tau}_{f,ij}\widetilde{(S_{ij})_{fa}} \\ &\quad - \tilde{\tau}_{f,ij}\widetilde{S}_{ij}'' - \tilde{\tau}_{in,ij}\widetilde{(S_{ij})_{fa}} - \tilde{\tau}_{in,ij}\widetilde{S}_{ij}'' \\ &\equiv \Pi_{mm,l} + \Pi_{mf,l} + \Pi_{fm,l} + \Pi_{ff,l} + \Pi_{inm,l} + \Pi_{inf,l}.\end{aligned} \tag{5.5}$$

Here S_{ij}'' is the strain-rate tensor in terms of the fluctuating velocities $\boldsymbol{u}''$, which is defined as $S_{ij}'' = (\partial u_i''/\partial x_j + \partial u_j''/\partial x_i)/2$.

On the basis of Helmholtz decomposition, $\tilde{\tau}_{f,ij}$ and S''_{ij} can be further decomposed into

$$\tilde{\tau}_{f,ij} = \tilde{\tau}_{fs,ij} + \tilde{\tau}_{fd,ij} + \tilde{\tau}_{fsd,ij},\ S''_{ij} = S''_{s,ij} + S''_{d,ij}, \tag{5.6}$$

where

$$\tilde{\tau}_{fs,ij} \equiv \bar{\rho}(\widetilde{u''_{s,i}u''_{s,j}} - \widetilde{u}''_{s,i}\widetilde{u}''_{s,j}), \tag{5.7}$$

$$\tilde{\tau}_{fd,ij} \equiv \bar{\rho}(\widetilde{u''_{d,i}u''_{d,j}} - \widetilde{u}''_{d,i}\widetilde{u}''_{d,j}), \tag{5.8}$$

$$\tilde{\tau}_{fsd,ij} \equiv \tilde{\tau}_{f,ij} - \tilde{\tau}_{fs,ij} - \tilde{\tau}_{fd,ij}, \tag{5.9}$$

$$S''_{s,ij} \equiv (\partial u''_{s,i}/\partial x_j + \partial u''_{s,j}/\partial x_i)/2, \tag{5.10}$$

$$S''_{d,ij} \equiv (\partial u''_{d,i}/\partial x_j + \partial u''_{d,j}/\partial x_i)/2. \tag{5.11}$$

Thus, two dominant components $\Pi_{fm,l} \equiv -\tilde{\tau}_{f,ij}\widetilde{(S_{ij})_{fa}}$ and $\Pi_{ff,l} \equiv -\tilde{\tau}_{f,ij}\widetilde{S}''_{ij}$ of the SGS flux of kinetic energy Π_l can be decomposed by

$$\begin{aligned}\Pi_{fm,l} &= -\tilde{\tau}_{fs,ij}\widetilde{(S_{ij})_{fa}} - \tilde{\tau}_{fd,ij}\widetilde{(S_{ij})_{fa}} - \tilde{\tau}_{fsd,ij}\widetilde{(S_{ij})_{fa}} \\ &\equiv \Pi_{fsm,l} + \Pi_{fdm,l} + \Pi_{fsdm,l}, \end{aligned} \tag{5.12}$$

$$\begin{aligned}\Pi_{ff,l} &= -\tilde{\tau}_{fs,ij}\widetilde{S}''_{s,ij} - \tilde{\tau}_{fs,ij}\widetilde{S}''_{d,ij} - \tilde{\tau}_{fd,ij}\widetilde{S}''_{s,ij} \\ &\quad - \tilde{\tau}_{fd,ij}\widetilde{S}''_{d,ij} - \tilde{\tau}_{fsd,ij}\widetilde{S}''_{s,ij} - \tilde{\tau}_{fsd,ij}\widetilde{S}''_{d,ij} \\ &\equiv \Pi_{fsfs,l} + \Pi_{fsfd,l} + \Pi_{fdfs,l} + \Pi_{fdfd,l} + \Pi_{fsdfs,l} + \Pi_{fsdfd,l}. \end{aligned} \tag{5.13}$$

The normalized streamwise–spanwise averages of the SGS flux of kinetic energy Π_l and its decomposed components in (5.5) along the wall-normal direction at filter widths $l/\delta_v = 75$ and 900 in M8T015 and M8T08 are depicted in figure 15. It is shown that at small scales $l/\delta_v = 75$, the component $\langle\Pi_{fm,l}\rangle_{xz}$ dominates in $\langle\Pi_l\rangle_{xz}$ and the component $\langle\Pi_{ff,l}\rangle_{xz}$ also plays a significant role in $\langle\Pi_l\rangle_{xz}$, while other components are negligible. Accordingly, $\langle\Pi_l\rangle_{xz}$ is mainly determined by the interaction between the fluctuating SGS stress $\tilde{\tau}_{f,ij}$ and the filtered strain-rate tensor $\widetilde{S}_{ij}$ at small scales. However, as the inertial range increases to $l/\delta_v = 900$, $\langle\Pi_l\rangle_{xz}$ is mainly dominated by the component $\langle\Pi_{fm,l}\rangle_{xz}$. The component $\langle\Pi_{ff,l}\rangle_{xz}$ is relatively small and other components are negligible. Thus, $\langle\Pi_l\rangle_{xz}$ is mainly dominated by the interaction between the fluctuating SGS stress $\tilde{\tau}_{f,ij}$ and the mean filtered strain-rate tensor $\widetilde{(S_{ij})_{fa}}$ in the inertial range. Moreover, $\langle\Pi_{fm,l}\rangle_{xz}$ attains its peak value in the buffer layer. The value of $\langle\Pi_{fm,l}\rangle_{xz}$ is positive, indicating that the interaction between the fluctuating SGS stress $\tilde{\tau}_{f,ij}$ and the mean filtered strain-rate tensor $\widetilde{(S_{ij})_{fa}}$ mainly leads to the direct transfer of kinetic energy from large scales to small scales. Moreover, it is shown that the magnitude of $\langle\Pi_{ff,l}\rangle_{xz}$ decreases as filter width increases, indicating that the positive and negative values of $\Pi_{ff,l}$ are largely cancelled in the inertial range.

According to the above observations, only $\Pi_{fm,l}/\varepsilon$ and $\Pi_{ff,l}/\varepsilon$ play significant roles in Π_l/ε. Therefore, we focus on $\Pi_{fm,l}/\varepsilon$ and $\Pi_{ff,l}/\varepsilon$ in further discussion.

The normalized streamwise–spanwise averages of $\Pi_{fm,l}$ and its decomposed components in (5.12) along the wall-normal direction at filter width $l/\delta_v = 900$ in M8T015 and M8T08 are shown in figure 16(*a*,*b*). It is found that $\langle\Pi_{fm,l}\rangle_{xz}$ is mainly dominated by its solenoidal component $\langle\Pi_{fsm,l}\rangle_{xz}$. Here $\langle\Pi_{fsm,l}\rangle_{xz}$ achieves its peak value in the buffer layer, indicating a strong intensity of fluctuating solenoidal kinetic energy transfer

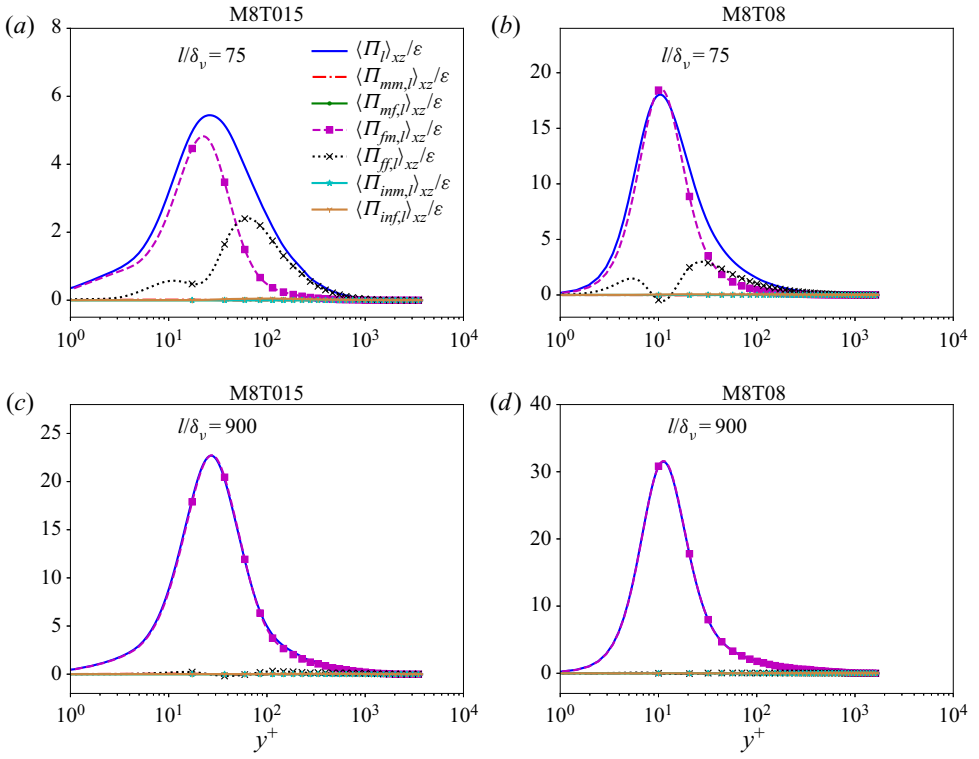

Figure 15. The normalized streamwise–spanwise averages of the SGS flux of kinetic energy Π_l and its decomposed components in (5.5) along the wall-normal direction at filter widths $l/\delta_v = 75$ and 900 in M8T015 and M8T08.

in this region. In the inertial range $l/\delta_v = 900$, $\langle \Pi_{fsm,l} \rangle_{xz}$ is even larger than $\langle \Pi_{fm,l} \rangle_{xz}$, and $\langle \Pi_{fsdm,l} \rangle_{xz}$ counteracts the contribution of the solenoidal component $\langle \Pi_{fsm,l} \rangle_{xz}$. The component $\langle \Pi_{fsdm,l} \rangle_{xz}$ achieves its peak value in the buffer layer, and its peak location is similar to that of $\langle \Pi_{fsm,l} \rangle_{xz}$. The dilatational component $\langle \Pi_{fdm,l} \rangle_{xz}$ is larger in M8T015 than in M8T08, indicating that the cold wall temperature enhances the compressibility effect. Also, $\langle \Pi_{fm,l} \rangle_{xz}$ in M8T015 is mainly dominated by the dilatational component $\langle \Pi_{fdm,l} \rangle_{xz}$ near the wall, while the solenoidal component $\langle \Pi_{fsm,l} \rangle_{xz}$ plays a predominant role far from the wall, implying that the cold wall temperature enhances the compressibility mainly in the near-wall region. Both $\langle \Pi_{fsm,l} \rangle_{xz}$ and $\langle \Pi_{fdm,l} \rangle_{xz}$ are positive, while $\langle \Pi_{fsdm,l} \rangle_{xz}$ is negative, indicating that the interaction between the fluctuating solenoidal SGS stress $\tilde{\tau}_{fs,ij}$ and the mean filtered strain-rate tensor $\widetilde{(S_{ij})_{fa}}$ as well as the interaction between the fluctuating dilatational SGS stress $\tilde{\tau}_{fd,ij}$ and the mean filtered strain-rate tensor $\widetilde{(S_{ij})_{fa}}$ mainly lead to the direct transfer of kinetic energy, while the interaction between $\tilde{\tau}_{fsd,ij}$ and $\widetilde{(S_{ij})_{fa}}$ mainly leads to the reverse transfer of kinetic energy.

The normalized streamwise–spanwise averages of $\Pi_{ff,l}$ and its decomposed components in (5.13) along the wall-normal direction at filter width $l/\delta_v = 900$ in M8T015 are shown in figure 16(*c*). It is found that the solenoidal component $\langle \Pi_{fsfs,l} \rangle_{xz}$ dominates in $\langle \Pi_{ff,l} \rangle_{xz}$. Other components have small contributions to $\langle \Pi_{ff,l} \rangle_{xz}$. In the inertial range $l/\delta_v = 900$, a strong local reverse fluctuating solenoidal kinetic energy transfer appears in the buffer layer.

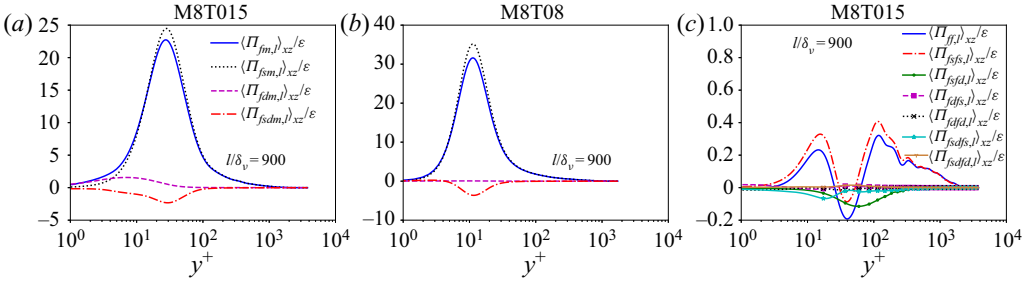

Figure 16. The normalized streamwise–spanwise averages of $\Pi_{fm,l}$ and its decomposed components in (5.12) along the wall-normal direction at filter widths $l/\delta_v = 900$ in (*a*) M8T015 and (*b*) M8T08. (*c*) The normalized streamwise–spanwise averages of $\Pi_{ff,l}$ and its decomposed components in (5.13) along the wall-normal direction at filter width $l/\delta_v = 900$ in M8T015.

The PDFs of the components $\Pi_{fm,l}/\varepsilon$ and $\Pi_{ff,l}/\varepsilon$ along the wall-normal direction in the inertial range $l/\delta_v = 900$ in M8T015 and M8T08 are shown in figure 17. The PDF of the component $\Pi_{fm,l}/\varepsilon$ is similar to that of Π_l/ε, and exhibits a strong positive skewness. Negative values of $\Pi_{fm,l}/\varepsilon$ only appear in M8T015, implying that the cold wall temperature enhances the local reverse kinetic energy transfer due to the interaction between the fluctuating SGS stress $\tilde{\tau}_{f,ij}$ and the mean filtered strain-rate tensor $\widetilde{(S_{ij})_{fa}}$. However, the PDF of $\Pi_{ff,l}/\varepsilon$ is slightly positively skewed and totally different from the PDFs of $\Pi_{fm,l}/\varepsilon$ and Π_l/ε, where strong intensities of negative values of $\Pi_{ff,l}/\varepsilon$ appear in both M8T015 and M8T08.

The PDFs of the components $\Pi_{fsm,l}/\varepsilon$, $\Pi_{fdm,l}/\varepsilon$ and $\Pi_{fsfs,l}/\varepsilon$ along the wall-normal direction in the inertial range $l/\delta_v = 900$ in M8T015 and M8T08 are shown in figure 18. The PDF of the component $\Pi_{fsm,l}/\varepsilon$ is similar to that of $\Pi_{fm,l}/\varepsilon$, and exhibits a strong positive skewness. Negative values of $\Pi_{fsm,l}/\varepsilon$ only exist in M8T015, implying that the cold wall temperature enhances the local reverse kinetic energy transfer due to the interaction between the fluctuating solenoidal SGS stress $\tilde{\tau}_{fs,ij}$ and the mean filtered strain-rate tensor $\widetilde{(S_{ij})_{fa}}$. Moreover, $\Pi_{fdm,l}/\varepsilon$ is positively skewed. The widest PDF of $\Pi_{fdm,l}/\varepsilon$ appears near the wall, indicating that the local transfer of fluctuating dilatational kinetic energy is concentrated in the near-wall region. The PDF of $\Pi_{fsfs,l}/\varepsilon$ is similar to that of $\Pi_{ff,l}/\varepsilon$. It is seen that $\Pi_{fsfs,l}/\varepsilon$ is slightly positively skewed, and strong intensities of negative values of $\Pi_{fsfs,l}/\varepsilon$ appear in the buffer layer, indicating the strong local reverse transfer of fluctuating solenoidal kinetic energy in this region.

Figures 19(*a*) and 19(*b*) show the conditional streamwise–spanwise average $\langle \Pi_{fm,l}/\varepsilon \mid \theta_l''^+ \rangle_{xz}$ and $\langle \Pi_{ff,l}/\varepsilon \mid \theta_l''^+ \rangle_{xz}$ along the wall-normal direction in the inertial range $l/\delta_v = 900$ in M8T015. The value of $\langle \Pi_{fm,l}/\varepsilon \mid \theta_l''^+ \rangle_{xz}$ is positive and increases as the magnitude of $\theta_l''^+$ increases, indicating that strong direct transfer caused by $\Pi_{fm,l}$ mainly appears in strong expansion and compression regions. Figure 19(*c*) shows the conditional streamwise–spanwise average $\langle \Pi_{ff,l}/\varepsilon \mid \theta_l''^+ \rangle_{xz}$ at $y^+ = 20$ for different filter widths $l/\delta_v = 750$, 900, 1050 and 1200 in M8T015. It is found that the conditional average $\langle \Pi_{ff,l}/\varepsilon \mid \theta_l''^+ \rangle_{xz}$ is nearly independent of filter width l/δ_v, especially in the weak compression and expansion regions at filter widths $l/\delta_v = 900$, 1050 and 1200 in the inertial range, which is similar to previous observations for compressible isotropic turbulence (Wang *et al.* 2018). However, in strong compression and expansion regions where the magnitude of the normalized fluctuating velocity divergence $\theta_l''^+$ is large, the

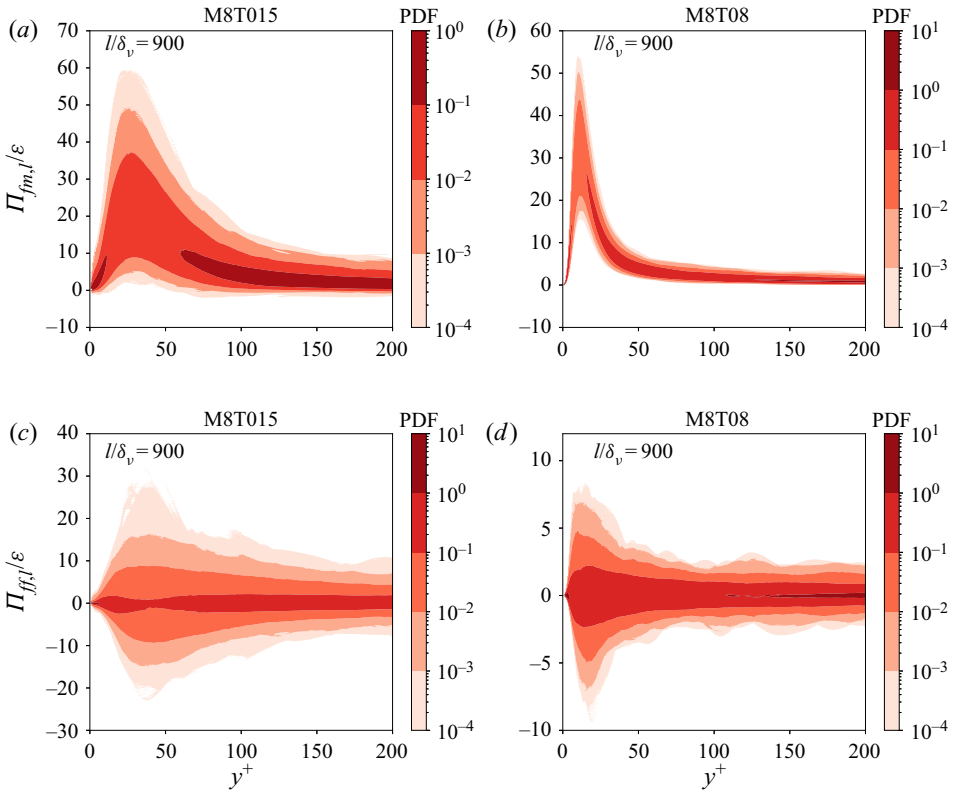

Figure 17. The PDFs of the components $\Pi_{fm,l}/\varepsilon$ and $\Pi_{ff,l}/\varepsilon$ along the wall-normal direction in the inertial range $l/\delta_v = 900$ in M8T015 and M8T08.

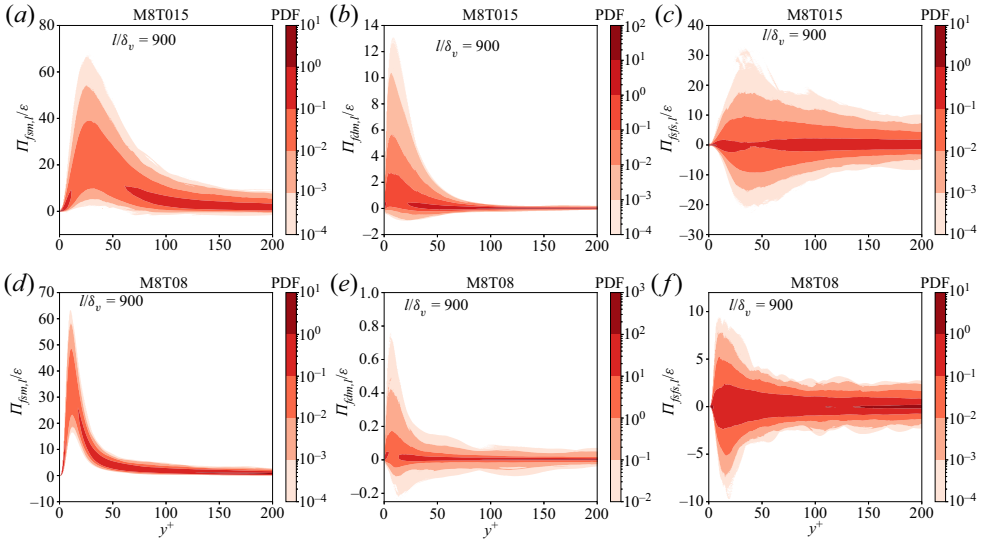

Figure 18. The PDFs of the components $\Pi_{fsm,l}/\varepsilon$, $\Pi_{fdm,l}/\varepsilon$ and $\Pi_{fsfs,l}/\varepsilon$ along the wall-normal direction in the inertial range $l/\delta_v = 900$ in M8T015 and M8T08.

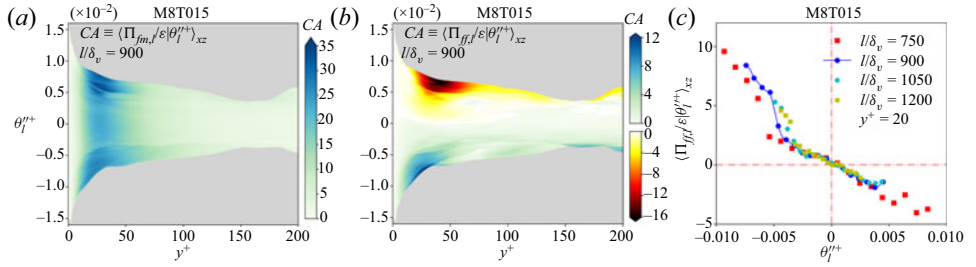

Figure 19. The streamwise–spanwise average of the component (*a*) $\Pi_{fm,l}/\varepsilon$ and (*b*) $\Pi_{ff,l}/\varepsilon$ conditioned on the normalized filtered fluctuating velocity divergence $\theta_l''^{+}$ along the wall-normal direction at filter width $l/\delta_v = 900$ in M8T015. (*c*) The streamwise–spanwise average of the component $\Pi_{ff,l}/\varepsilon$ conditioned on the normalized filtered fluctuating velocity divergence $\theta_l''^{+}$ at $y^+ = 20$ for different filter widths $l/\delta_v = 750$, 900, 1050 and 1200 in M8T015.

values of $\langle \Pi_{ff,l}/\varepsilon \mid \theta_l''^{+} \rangle_{xz}$ are quite scattered mainly due to the lack of samples. The observation of the scale-invariant property of the conditional average $\langle \Pi_{ff,l}/\varepsilon \mid \theta_l''^{+} \rangle_{xz}$ is consistent with the well-known energy cascade hypothesis (Meneveau & Katz 2000; Pope 2000). In the inertial range, the inter-scale transfer of kinetic energy as well as the conditional average of normalized SGS flux are nearly scale-invariant. It is shown that positive values of $\langle \Pi_{ff,l}/\varepsilon \mid \theta_l''^{+} \rangle_{xz}$ often appear in compression regions, while negative values of $\langle \Pi_{ff,l}/\varepsilon \mid \theta_l''^{+} \rangle_{xz}$ often exist in expansion regions, which implies that compression motions have a major contribution to the direct transfer of fluctuating kinetic energy, while expansion motions play a significant role in the reverse transfer of fluctuating kinetic energy. This observation is consistent with the phenomenon in compressible isotropic turbulence (Wang *et al.* 2018).

6. Summary and conclusion

In this paper, the filtering method is applied to investigate the kinetic energy transfer in a hypersonic turbulent boundary layer for different Mach numbers and wall temperature ratios. The effects of compressibility and wall temperature on the kinetic energy transfer and the SGS flux of kinetic energy are systematically discussed. Among three typical transformations of mean velocity profiles, the transformation of Volpiani *et al.* (2020) exhibits the best results, and obeys both the same linear law and log law as in incompressible wall-bounded flows. A colder wall temperature with a stronger wall temperature gradient results in a stronger wall heat flux, which further gives rise to a stronger compressibility effect near the wall.

The streamwise–spanwise average values of inter-scale kinetic energy transfer terms are discussed. The average filtered spatial convection term $\langle J_l \rangle_{xz}/\varepsilon$ and average filtered viscous dissipation term $\langle D_l \rangle_{xz}/\varepsilon$ are dominant in the near-wall region, and decrease rapidly away from wall. However, the average filtered pressure dilatation term $\langle \Phi_l \rangle_{xz}/\varepsilon$ is negligibly small along the wall-normal direction at large scales, indicating that the net contribution of pressure dilatation to the average kinetic energy is negligibly small at large scales. The average SGS flux of kinetic energy $\langle \Pi_l \rangle_{xz}/\varepsilon$ increases from zero as the filter width l/δ_v increases from the Kolmogorov scale to the inertial range, and achieves its peak value in the buffer layer. The behaviours of inter-scale kinetic energy transfer terms are consistent with the kinetic energy cascade scenario.

The PDF of the normalized SGS flux Π_l/ε exhibits a strong positive skewness. It is found that a cold wall temperature enhances the local reverse transfer of kinetic energy from small scales to large scales, and suppresses the local direct transfer of kinetic energy from large scales to small scales. It is also shown that the effect of wall temperature is more prominent at small scales.

The effect of local compressibility is further examined by the conditional average of normalized SGS flux with respect to the filtered velocity divergence. It is found that the direct transfer of kinetic energy is dominant in the hypersonic turbulent boundary layer, and the local reverse transfer of kinetic energy is mainly concentrated in the expansion region. Moreover, the wall, especially with cold wall temperature, can suppress the efficiency of inter-scale kinetic energy transfer.

Mean-fluctuating decomposition and Helmholtz decomposition on SGS flux of kinetic energy are introduced. The streamwise–spanwise average of the SGS flux of kinetic energy $\langle\Pi_l\rangle_{xz}$ is mainly determined by the interaction between the fluctuating SGS stress $\tilde{\tau}_{f,ij}$ and the filtered strain-rate tensor $\widetilde{S}_{ij}$ at small scales, while only $\langle\Pi_{fm,l}\rangle_{xz}$ is dominant in $\langle\Pi_l\rangle_{xz}$ in the inertial range. The value of $\langle\Pi_{fm,l}\rangle_{xz}$ is positive along the wall-normal direction and mainly dominated by its solenoidal component $\langle\Pi_{fsm,l}\rangle_{xz}$. A strong transfer of the solenoidal component of fluctuating kinetic energy due to $\Pi_{fsm,l}$ is identified in the buffer layer, while a significant transfer of the dilatational component of fluctuating kinetic energy due to $\Pi_{fdm,l}$ is observed in the near-wall region. In the inertial range, $\langle\Pi_{ff,l}\rangle_{xz}$ is dominated by its solenoidal component $\langle\Pi_{fsfs,l}\rangle_{xz}$, and exhibits a negative peak value in the buffer layer, indicating a strong local reverse transfer of fluctuating kinetic energy in this region. Conditional streamwise–spanwise average $\langle\Pi_{ff,l}/\varepsilon \mid \theta_l''^{+}\rangle_{xz}$ illustrates that compression motions have a major contribution to the direct transfer of fluctuating kinetic energy, while expansion motions play a significant role in the reverse transfer of fluctuating kinetic energy.

In conclusion, the various effects of the wall temperature and compressibility on the SGS flux of kinetic energy in a hypersonic turbulent boundary layer are revealed. The cold wall temperature significantly enhances the compressibility in the near-wall region and a local reverse SGS flux of kinetic energy in the strong expansion region, which should be considered in the LES modelling of hypersonic turbulent boundary layers.

Funding. This work was supported by the National Natural Science Foundation of China (NSFC grant nos. 91952104, 92052301 and 91752201), by the NSFC Basic Science Center Program (grant no. 11988102), by the Technology and Innovation Commission of Shenzhen Municipality (grant nos. KQTD20180411143441009 and JCYJ20170412151759222) and by the Department of Science and Technology of Guangdong Province (grant no. 2019B21203001). This work was also supported by the Center for Computational Science and Engineering of Southern University of Science and Technology.

Declaration of interest. The authors report no conflict of interest.

Author ORCIDs.
Dehao Xu https://orcid.org/0000-0003-2442-4150;
Jianchun Wang https://orcid.org/0000-0001-5101-7791;
Changping Yu https://orcid.org/0000-0002-2126-1344.

References

Alizard, F., Pirozzoli, S., Bernardini, M. & Grasso, F. 2015 Optimal transient growth in compressible turbulent boundary layers. *J. Fluid Mech.* **770**, 124–155.

Aluie, H. 2011 Compressible turbulence: the cascade and its locality. *Phys. Rev. Lett.* **106**, 174502.

Aluie, H. 2013 Scale decomposition in compressible turbulence. *Phys.* D **247**, 2013.

ALUIE, H. & EYINK, G.L. 2009 Localness of energy cascade in hydrodynamic turbulence. II. Sharp spectral filter. *Phys. Fluids* **21**, 115108.

ALUIE, H., LI, S. & LI, H. 2012 Conservative cascade of kinetic energy in compressible turbulence. *Astrophys. J. Lett.* **751**, L29.

ANDERSON, J.D. 2006 *Hypersonic and High-Temperature Gas Dynamics*. American Institute of Aeronautics and Astronautics.

BALSARA, D.S. & SHU, C. 2000 Monotonicity preserving weighted essentially non-oscillatory schemes with increasingly high order of accuracy. *J. Comput. Phys.* **160**, 405–452.

BRADSHAW, P. 1977 Compressible turbulent shear layers. *Annu. Rev. Fluid Mech.* **9**, 33–54.

CEBECI, T. & SMITH, A.M.O. 1974 *Analysis of Turbulent Boundary Layers*. Academic.

CERUTTI, S. & MENEVEAU, C. 1998 Intermittency and relative scaling of subgrid-scale energy dissipation in isotropic turbulence. *Phys. Fluids* **10**, 928–937.

CHEN, S., WANG, J., LI, H., WAN, M. & CHEN, S. 2018 Spectra and Mach number scaling in compressible homogeneous shear turbulence. *Phys. Fluids* **30**, 065109.

CHEN, S., WANG, J., LI, H., WAN, M. & CHEN, S. 2019*a* Effect of compressibility on small scale statistics in homogeneous shear turbulence. *Phys. Fluids* **31**, 025107.

CHEN, S., WANG, X., WANG, J., LI, H., WAN, M. & CHEN, S. 2019*b* Effects of bulk viscosity on compressible homogeneous turbulence. *Phys. Fluids* **31**, 085115.

CHEN, L., XU, C. & LU, X. 2010 Numerical investigation of the compressible flow past an aerofoil. *J. Fluid Mech.* **643**, 97–126.

CHU, Y. & LU, X. 2013 Topological evolution in compressible turbulent boundary layers. *J. Fluid Mech.* **733**, 414–438.

CHU, Y., ZHUANG, Y. & LU, X. 2013 Effect of wall temperature on hypersonic turbulent boundary layer. *J. Turbul.* **14**, 37–57.

DOMARADZKI, J.A., LIU, W. & BRACHET, M.E. 1993 An analysis of subgrid-scale interactions in numerically simulated isotropic turbulence. *Phys. Fluids* A*: Fluid Dyn.* **5**, 1747–1759.

DUAN, L., BEEKMAN, I. & MARTIN, M.P. 2010 Direct numerical simulation of hypersonic turbulent boundary layers. Part 2. Effect of wall temperature. *J. Fluid Mech.* **655**, 419–445.

DUAN, L., BEEKMAN, I. & MARTIN, M.P. 2011 Direct numerical simulation of hypersonic turbulent boundary layers. Part 3. Effect of mach number. *J. Fluid Mech.* **672**, 245–267.

ERM, L.P. & JOUBERT, P.N. 1991 Low-Reynolds-number turbulent boundary layers. *J. Fluid Mech.* **230**, 1–44.

EYINK, G.L. 2005 Locality of turbulent cascades. *Phys.* D*: Nonlinear Phenom.* **207**, 91–116.

EYINK, G.L. & ALUIE, H. 2009 Localness of energy cascade in hydrodynamic turbulence. I. Smooth coarse graining. *Phys. Fluids* **21**, 115107.

GATSKI, T.B. & BONNET, J.P. 2009 *Compressibility, Turbulence and High Speed Flow*. Elsevier.

GUARINI, S.E., MOSER, R.D., SHARIFF, K. & WRAY, A. 2000 Direct numerical simulation of a supersonic turbulent boundary layer at Mach 2.5. *J. Fluid Mech.* **414**, 1–33.

HAMMAN, C.W., KLEWICKI, J.C. & KIRBY, R.M. 2008 On the lamb vector divergence in Navier–Stokes flows. *J. Fluid Mech.* **610**, 261–284.

HIRASAKI, G. & HELLUMS, J. 1970 Boundary conditions on the vector and scalar potentials in viscous three-dimensional hydrodynamics. *Q. Appl. Maths* **28**, 293–296.

HOWE, M.S. 1975 Contributions to the theory of aerodynamic sound, with application to excess jet noise and the theory of the flute. *J. Fluid Mech.* **71**, 625–673.

JAGANNATHAN, S. & DONZIS, D.A. 2016 Reynolds and Mach number scaling in solenoidally-forced compressible turbulence using high-resolution direct numerical simulations. *J. Fluid Mech.* **789**, 669–707.

JOSYULA, E. 2015 *Hypersonic Nonequilibrium Flows: Fundamentals and Recent Advances*. American Institute of Aeronautics and Astronautics.

KERR, R.M., DOMARADZKI, J.A. & BARBIER, G. 1996 Small-scale properties of nonlinear interactions and subgrid-scale energy transfer in isotropic turbulence. *Phys. Fluids* **8**, 197–208.

LAGHA, M., KIM, J., ELDREDGE, J.D. & ZHONG, X. 2011 A numerical study of compressible turbulent boundary layers. *Phys. Fluids* **23**, 015106.

LI, Q. & COLEMAN, G.N. 2012 *DNS of an Oblique Shock Wave Impinging upon a Turbulent Boundary Layer*. Springer.

LI, X., FU, D. & MA, Y. 2008 Direct numerical simulation of hypersonic boundary layer transition over a blunt cone. *AIAA J.* **46**, 2899–2913.

LI, X., TONG, F., YU, C. & LI, X. 2019 Statistical analysis of temperature distribution on vortex surfaces in hypersonic turbulent boundary layer. *Phys. Fluids* **31**, 106101.

LIANG, X. & LI, X. 2013 DNS of a spatially evolving hypersonic turbulent boundary layer at Mach 8. *Sci. China Phys. Mech. Astron.* **56**, 1408–1418.

LIANG, X. & LI, X. 2015 Direct numerical simulation on Mach number and wall temperature effects in the turbulent flows of flat-plate boundary layer. *Commun. Comput. Phys.* **17**, 189–212.

LIGHTHILL, M.J. 1952 On sound generated aerodynamically. Part I. General theory. *Proc. R. Soc. Lond.* A **211**, 564–587.

MAEDER, T., ADAMS, N.A. & KLEISER, L. 2001 Direct simulation of turbulent supersonic boundary layers by an extended temporal approach. *J. Fluid Mech.* **429**, 187–216.

MARCO, A., CAMUSSI, R., BERNARDINI, M. & PIROZZOLI, S. 2013 Wall pressure coherence in supersonic turbulent boundary layers. *J. Fluid Mech.* **732**, 445–456.

MARTIN, M.P. 2007 Direct numerical simulation of hypersonic turbulent boundary layers. Part 1. Initialization and comparison with experiments. *J. Fluid Mech.* **570**, 347–364.

MARTIN, M.P., PIOMELLI, U., CANDLER, G.V. & HUSSAINI, M.Y. 2000 Subgrid-scale models for compressible large-eddy simulations. *Theor. Comput. Fluid Dyn.* **13**, 361–376.

MENEVEAU, C. & KATZ, J. 2000 Scale-invariance and turbulence models for large-eddy simulation. *Annu. Rev. Fluid Mech.* **32**, 1–32.

MODESTI, D. & PIROZZOLI, S. 2016 Reynolds and mach number effects in compressible turbulent channel flow. *Intl J. Heat Fluid Flow* **59**, 33–49.

PIOMELII, U., CABOT, W.H., MOIN, P. & LEE, S. 1991 Subgrid-scale backscatter in turbulent and transitional flows. *Phys. Fluids* A **3**, 1766–1771.

PIROZZOLI, S. 2012 On the size of the energy-containing eddies in the outer turbulent wall layer. *J. Fluid Mech.* **702**, 521–532.

PIROZZOLI, S. & BERNARDINI, M. 2011 Turbulence in supersonic boundary layers at moderate Reynolds number. *J. Fluid Mech.* **688**, 120–168.

PIROZZOLI, S., BERNARDINI, M. & GRASSO, F. 2008 Characterization of coherent vortical structures in a supersonic turbulent boundary layer. *J. Fluid Mech.* **613**, 205–231.

PIROZZOLI, S., BERNARDINI, M. & GRASSO, F. 2010 On the dynamical relevance of coherent vortical structures in turbulent boundary layers. *J. Fluid Mech.* **648**, 325–349.

PIROZZOLI, S., GRASSO, F. & GATSKI, T.B. 2004 Direct numerical simulation and analysis of a spatially evolving supersonic turbulent boundary layer at $M = 2.25$. *Phys. Fluids* **16**, 530–545.

POPE, S.B. 2000 *Turbulent Flows*. Cambridge University Press.

RINGUETTE, M., WU, M. & MARTIN, M.P. 2008 Coherent structures in direct numerical simulation of turbulent boundary layers at Mach 3. *J. Fluid Mech.* **594**, 59–69.

SHE, Z., ZOU, H., XIAO, M., CHEN, X. & HUSSAIN, F. 2018 Prediction of compressible turbulent boundary layer via a symmetry-based length model. *J. Fluid Mech.* **857**, 449–468.

SIMENS, M.P., JIMÉNEZ, J., HOYAS, S. & MIZUNO, Y. 2009 A high-resolution code for turbulent boundary layers. *J. Comput. Phys.* **228**, 4218–4231.

SMITS, A.J. & DUSSAUGE, J.P. 2006 *Turbulent Shear Layers in Supersonic Flow*. Springer.

TENG, J., WANG, J., LI, H. & CHEN, S. 2020 Spectra and scaling in chemically reacting compressible isotropic turbulence. *Phys. Rev. Fluids* **5**, 084601.

TENG, J., WANG, J., LI, H. & CHEN, S. 2021 Inter-scale kinetic energy transfer in chemically reacting compressible isotropic turbulence. *J. Fluid Mech.* **912**, A36.

TRETTEL, A. & LARSSON, J. 2016 Mean velocity scaling for compressible wall turbulence with heat transfer. *Phys. Fluids* **28**, 026102.

VAN DRIEST, E.R. 1951 Turbulent boundary layer in compressible fluids. *J. Aeronaut. Sci.* **18** (3), 145–160.

VOLPIANI, P., IYER, P., PIROZZOLI, S. & LARSSON, J. 2020 Data-driven compressibility transformation for turbulent wall layers. *Phys. Rev. Fluids* **5**, 052602(R).

WANG, J., SHI, Y., WANG, L., XIAO, Z., HE, X. & CHEN, S. 2012*a* Effect of compressibility on the small-scale structures in isotropic turbulence. *J. Fluid Mech.* **713**, 588–631.

WANG, J., SHI, Y., WANG, L., XIAO, Z., HE, X. & CHEN, S. 2012*b* Scaling and statistics in three-dimensional compressible turbulence. *Phys. Rev. Lett.* **108**, 214505.

WANG, J., WAN, M., CHEN, S. & CHEN, S. 2018 Kinetic energy transfer in compressible isotropic turbulence. *J. Fluid Mech.* **841**, 581–613.

WANG, J., WAN, M., CHEN, S., XIE, C., ZHENG, Q., WANG, L. & CHEN, S. 2020 Effect of flow topology on the kinetic energy flux in compressible isotropic turbulence. *J. Fluid Mech.* **883**, A11.

WANG, J., YANG, Y., SHI, Y., XIAO, Z., HE, X. & CHEN, S. 2013 Cascade of kinetic energy in three-dimensional compressible turbulence. *Phys. Rev. Lett.* **110**, 214505.

WANG, L. & LU, X. 2012 Flow topology in compressible turbulent boundary layer. *J. Fluid Mech.* **703**, 255–278.

WHITE, F.M. 2006 *Viscous Fluid Flow*, 3rd edn. McGraw-Hill.

XU, D., WANG, J., WAN, W., YU, C., LI, X. & CHEN, S. 2021 Compressibility effect in hypersonic boundary layer with isothermal wall condition. *Phys. Rev. Fluids* **6**, 054609.

YU, M. & XU, C. 2021 Compressibility effects on hypersonic turbulent channel flow with cold walls. *Phys. Fluids* **33**, 075106.

YU, M., XU, C. & PIROZZOLI, S. 2019 Genuine compressibility effects in wall-bounded turbulence. *Phys. Rev. Fluids* **4**, 123402.

ZHANG, C., DUAN, L. & CHOUDHARI, M. 2018 Direct numerical simulation database for supersonic and hypersonic turbulent boundary layers. *AIAA J.* **56**, 4297–4311.

ZHANG, Y., BI, W., HUSSAIN, F., LI, X. & SHE, Z. 2012 Mach-number-invariant mean-velocity profile of compressible turbulent boundary layers. *Phys. Rev. Lett.* **109**, 054502.

ZHANG, Y., BI, W., HUSSAIN, F. & SHE, Z. 2014 A generalized Reynolds analogy for compressible wall-bounded turbulent flows. *J. Fluid Mech.* **739**, 392–420.

ZHENG, W., RUAN, S., YANG, Y., HE, L. & CHEN, S. 2019 Image-based modelling of the skin-friction coefficient in compressible boundary-layer transition. *J. Fluid Mech.* **875**, 1175–1203.

ZHENG, Q., WANG, J., NOACK, B.R., LI, H., WAN, M. & CHEN, S. 2020 Vibrational relaxation in compressible isotropic turbulence with thermal non-equilibrium. *Phys. Rev. Fluids* **5**, 044602.

ZHENG, Q., WANG, J., NOACK, B.R., MAHBUB, A., LI, H. & CHEN, S. 2021 Transfer of internal energy fluctuation in compressible isotropic turbulence with vibrational nonequilibrium. *J. Fluid Mech.* **919**, A26.